Engineering Analysis with Boundary Elements 135 (2022) 93–114

Contents lists available at ScienceDirect

Engineering Analysis with Boundary Elements

journal homepage: www.elsevier.com/locate/enganabound

Inclusion-based boundary element method for virtual experiments of particulate composites containing arbitrarily shaped inhomogeneities

Chunlin Wu [a], Liangliang Zhang [a,b], Gan Song [a], Huiming Yin [a,*]

[a] Department of Civil Engineering and Engineering Mechanics, Columbia University, 610 Seeley W. Mudd 500 West 120th Street, NY, 10027, United States of America

[b] Department of Applied Mechanics, China Agricultural University, Beijing, 100083, China

ARTICLE INFO

Keywords:
Eshelby's equivalent inclusion method
Boundary element method (BEM)
Inclusion and inhomogeneity
Green's function
Microstructure

ABSTRACT

This paper extends our recent work [1] to evaluate the elastic fields and effective modulus of a composite containing arbitrarily shaped inhomogeneities for both two-dimensional (2D) and three-dimensional (3D) problems. Based on Eshelby's equivalent inclusion method (EIM), the material mismatch between inhomogeneities and matrix phases is represented with a continuously distributed eigenstrain on inclusions. Since there exists singularities at the vertices of polyhedral inhomogeneities, domain discretization of inhomogeneities is used to interpolate the eigenstrain distribution, and high accuracy is obtained by using the closed-form integrals of the source field. The influence of the singularity decays in $\frac{1}{r^2}$ and $\frac{1}{r^3}$ for 2D and 3D problems respectively. Because Eshelby's tensors depend on the shape instead of the size, the iBEM is particularly suitable for cross scale modeling of composites with a wide range of particle sizes. Although a number of elements are required to provide high fidelity results of the local field around the vertices, in general, very few elements or a single element are enough for each inhomogeneity to obtain the convergent solutions of the effective material properties, which enables virtual experiments of a composite containing many inhomogeneities. This novel numerical method has been verified with the finite element method (FEM) with much more elements. Virtual experiments of composites with many particles demonstrate its versatile capability and great potentials.

1. Introduction

Considering an infinitely extended matrix embedded with one ellipsoidal subdomain with different elastic modulus (inhomogeneity) under far-field stress, Eshelby [2] proposed to substitute the sub-domain by the same material as the matrix but with continuous inelastic strain field, namely eigenstrain, to represent the stress disturbance caused by the material mismatch, which is called the equivalent inclusion method (EIM). With the equivalent stress conditions of the inhomogeneity, the eigenstrain field could be determined and superposed with the far-field stress to obtain the entire elastic fields. Since the explicit volume/area integral of the Green's function for ellipsoidal or elliptical inclusions are available in literature, the EIM is intensively applied to investigate the disturbed stress field [3–5]. Shodja et al. [6] combined the EIM and Hill's theorem to determine the stress intensity factors of cracks with arbitrary orientation under non-uniformed far-field stress. Jin et al. [7] investigated the stress field and displacement field of the elliptical inclusion with the closed-form solution.

Based on the strain gradient theory, Ma and Gao [8,9] derived the analytical strain-gradient Eshelby's tensor for elliptical/ellipsoidal inclusions. For the conventional Eshelby's second problem, the eigenstrain field is constant over the inhomogeneity because the volume's integral of Green's function is constant. Several factor, however, may lead to the non-uniformity of the eigenstrain field, such as, interactions between inhomogeneities [1,4–6], interactions between inhomogeneities and boundary [10–12],micro-structural dependent size effect [8,9,13], shape effect [14–17] and various loading conditions [1,4,11,18].

Although the EIM has been successfully applied to the ellipsoidal/elliptical inhomogeneities, for polygonal inclusions, a number of pioneering works on the classic Eshelby's tensor can be found in the literature [13,19–25] for inclusion problems with a prescribed eigenstrain only. For inhomogeneity problems, the eigenstrain distributed needs to be solved by the EIM, the Eshelby's tensor for a constant eigenstrain is not sufficient because the mismatch eigenstrain will obviously not be uniform due to the non-uniformity of Eshelby's tensor. Recently, Wu and Yin [26,27] derived the solution for a polynomial form of eigenstrain and used EIM to solve for the elastic fields of an infinite domain containing polygonal/polyhedral inhomogeneities.

* Corresponding author.
E-mail addresses: cw3056@columbia.edu (C. Wu), llzhang@cau.edu.cn (L. Zhang), gs2683@columbia.edu (G. Song), yin@civil.columbia.edu (H. Yin).

https://doi.org/10.1016/j.enganabound.2021.10.024
Received 14 August 2021; Received in revised form 1 October 2021; Accepted 19 October 2021
Available online 26 November 2021

However, there are two challenging issues to apply the method directly [28,29] for actual experiments of composites with arbitrary shaped of inhomogeneities:

(1) Singularity effects exists on the edges of the polyhedron, vertices for polygon and polyhedron. The assumption of single polynomial form of eigenstrain over the inhomogeneity domain cannot capture the local solution accurately.

(2) Actual composites samples exhibit a certain size (finite domain), the interactions between inhomogeneities and the boundary cannot be quantified.

To improve the accuracy of the EIM on polygonal/polyhedral inhomogeneities, two general approaches were used in the literature: (i) increase the order of eigenstrain field [4,5,26] or the strain field [13], and (ii) discretization over the inhomogeneities with small/elementary elements [30–32]. As for the first approach, based on the continuity of the eigenstrain field, it could be expanded in Taylor series [5]. However, Wu and Yin [26,27] have shown that even with the quadratic order eigenstrain, the prediction of stress fields of one triangular/tetrahedral inhomogeneity under uniform far-field load may not be accurate enough due to the singularity. It is not effective to use a single polynomial function to approximate the eigenstrain distribution accurately. Regarding to the second approach, Nakasone et al. [30] and Hou [32] et al. discretized the inhomogeneity domain with triangular elements and apply the numerical EIM. Zhou et al. [31] discretized the subdomain with small enough rectangular elements, where the eigenstrain field is approximated by a piecewise uniform function. A certain level of agreement was obtained in their work. The continuity of eigenstrain, however, is lost under the assumption of uniform eigenstrain in the basic elements. In addition, even had the assumption be acceptable with small elements, to approach the boundary of the polygonal/polyhedral subdomains may lead to a dramatic increase of the number of elements, which causes inefficiency of computation. It is the first time in this paper to use the analytical Eshelby's tensor for piece-wise continuous eigenstrain at the C^0 continuity for a high accuracy and rapid convergence to the exact solution by refining the mesh.

For the second challenging issue of the finite domain, it is important to consider the boundary effect on the local field because different loads can be applied to the boundary in physical experiments and an actual specimen always exhibits a finite size. The infinite domain is a theoretical assumption. To reproduce physical experiments in a computer, the inclusion-based boundary element method (iBEM) combines the EIM and BEM [1,11,33] to consider the effects from both the inhomogeneities and boundary. The advantages of iBEM are as follows: (1) For ellipsoidal or elliptical inhomogeneities, no internal mesh is required either for the matrix nor for the subdomains, and a polynomial eigenstrain can provide tailorable accuracy to the exact solution. (2) For arbitrary polygonal/polyhedral inhomogeneities, a piece-wise eigenstrain on a discretized inhomogeneity ensures the high accuracy with the C^0 continuity of the eigenstrain field. Refining particle discretization can approach the exact solution for the inhomogeneity problems. (3) Because no mesh is required in the matrix, and Eshelby tensors on inhomogeneities are size independent, the ill-conditioned mesh is avoided, and the size gradation of inhomogeneities could be simulated given the dimensions and locations. Notice that although the ellipsoidal or elliptical inhomogeneities have been simulated with traditional Eshelby's tensors [1], it can also be reproduced by a number of polyhedrons or polygons numerically [26] or represented by the integral of infinitesimal polygonal/polyhedral elements analytically.

With the above advantages, the iBEM is particularly suitable for modeling the effective material behavior containing a large variety of inhomogeneities in size, shape, and material properties. It can be used for particle interaction crossing size-scales and virtual experiments of a physical composite specimen. It can predict both the local field and non-local behavior of a composite specimen. We compare the iBEM with the existing methods in the literature as follows:

(1) The EIM has been applied to simulate the elastic fields of ellipsoidal or elliptical inhomogeneities, which served as the foundation for several micromechanics models, i.e, Mori–Tanaka method, the self-consistent scheme, and the dilute model [33–35] using various homogenization assumptions without directly considering the boundary effect and the effect of particle–particle interactions. The iBEM easily addressed the boundary effect by the boundary integral, moreover, it extended the particle shape to arbitrary shapes of inhomogeneities. Hence, iBEM is not only applicable to micromechanics, but also serves a versatile computational method for materials or structures with heterogeneous microstructure.

(2) Due to the limitations of micromechanics models, several numerical methods were developed to conduct the virtual experiments of composite under various boundary conditions (BC). In the previous work, the traditional BEM adopts the multi-region [36–38], which meshes the boundary of subdomains and collocate the boundary nodes with continuity conditions of tractions and displacements. Proposed by Beer [39], the major disadvantage of the multi-region method is the introduction of additional equations and unknowns to the linear system of equations. Therefore, it is expensive and uncertain to obtain the stable and convergent solution for angular shape of particles, particularly for a large number of particles. The present iBEM uses the same fundamental solution for the whole domain with stress equivalence and avoids the interface continuity equations.

(3) Helsing [40] proposed an adaptive algorithm based on the Fredholm's integral equation for multiple cracks and investigated the effective elastic properties under 10,000 cracks in 2D problem. Fu et al. [41], Fu and Rodin [42] and Lai and Rodin [43] developed the fast Galerkin BEM for domain containing many particles. Liu [44] and Liu and Shen [45] applied the fast multipole algorithm. Wu et al. [46] extended it for two-dimensional nonlinear interface debonding problem. Although the fast multipole method (FMM) can significantly save the computational cost, it still relies on the interface continuity equations for the multi-region domain. On the contrary, the iBEM can use very few or even merely one element for each particle with analytical integral of particle domain to achieve high accuracy. The concept of FMM has also been used in iBEM to define an influence zone or particle interaction cutoff given a certain error limit, so that iBEM can theoretically achieve the same level of computational efficiency.

(4) To avoid the multi-region issue, the revised boundary-domain [47], eigen-field based boundary integral equations [8,48,49] are proposed. The dual reciprocity BEM (DRBEM), introduced by Nardini and Brebbia [50], avoids the volume/area integral of non-homogeneous terms (i.e, body force) through approximation with basis functions [51,52]. Although DRBEM could solve the problem with BEM in original form, its numerical accuracy is highly determined by selections of basis functions, locations of the domain points [39,53]. Ingber et al. [54] conducted a comparison of domain integral with the DRBEM and particular solution method, and proved better accuracy for method with domain integral. However, all those methods rely on the numerical integrals over the particle, which bring difficulties for different shapes of particles. For example, a spherical particle needs a lot of linear elements to match the geometry. The iBEM integrates the analytical domain integral for ellipsoidal/elliptical and polyhedral/polygonal particles into the computation and represents the highest accuracy for the domain integral.

(5) Another extension of the FEM/BEM is the combination of isogeometric analysis (IGA) [55], namely IGAFEM [56–58] and IGABEM [39,59–62], whose advantage is the seamless integration with CAD. Beer et al. [39,63] proposed an iterative scheme to simulate the inclusion problem, which converts the mismatch initial stress to body force and traction increments. And such body force increments in a general inclusion could only be treated by numerical domain integral of the Green's function. Compared with FEM or FVM, iBEM exhibits advantages in a much lower degree of freedom (DOF); different from IGABEM [63],

the iBEM is based on the closed-form area (2D) or volume (3D) integrals of the Green's function and avoids the numerical stability and convergence in iterations.

(6) Moreover, besides the BEM, most numerical methods require the discretization of the entire domain, such as finite element method (FEM) and finite volume method (FVM). Sukumar et al. [64] and Du et al. [65] proposed the extended finite element method (xFEM) to solve the inhomogeneity problems, in which the FEM approximation is enriched by additional discontinuous functions. Benowitz and Waisman [66] later used the numerical spline-based enrichment function with inclusion internal boundary discretization. The iBEM contains the singularity in the Eshelby's tensor as well, but only the integral over the particle is required. Therefore, much fewer degrees of freedom is needed to solve the problem.

Particularly, the iBEM is suitable for cross-scale modeling and simulation because the Eshelby's tensor is size independent and dimensionless. It can predict the effective material performance with a given microstructure conveniently because the traction and displacement on the boundary are the principal variables to solve [1]. As the effective material behaviors do change with the shapes (i.e, aspect ratio, orientations), size gradation (i.e, dimension) and distribution of the inhomogeneities, the iBEM can capture the difference caused by these microstructural features. The iBEM's using analytical integrals on inhomogeneities can avoid the numerical integral issues and provide higher accuracy in comparison with the above BEM methods.

Overall, the iBEM integrates the boundary integral equation (BIE) and equivalent inclusion method (EIM) [1] to solve the inhomogeneity problem for a number of particles embedded in a matrix with certain loads on the boundary or inhomogeneities. As the extension, although the ellipsoidal/elliptical geometry is versatile, this paper enables the simulation of arbitrary shaped polygonal/polyhedral inhomogeneities by the domain discretization method, which is the main limitation in our previous work [1]. Section 2 formulates the closed-form Eshelby's tensor for arbitrary polygonal/polyhedral inclusions based on the shape functions; whereas Eshelby's tensor for elliptical inclusions have already existed in the literature [1,4]. Subsequently, the numerical implementation of the inclusion-based boundary element method (iBEM) is presented. In Section 3, the iBEM is verified with the FEM results for the convergence performance and accuracy. Thanks to the closed-form domain integral, only 1 element for the inclusion can provide the exact solution for the unbounded domain and high fidelity solution for bounded domain with iBEM. For inhomogeneity problems, the iBEM exhibits a high convergent rate as well. Section 4 illustrates inhomogeneity problems with the case studies of close interactions of multiple particles and boundary. The singularity of eigenstrain and its influence zone on the stress distribution is discussed as well. In Section 5, the virtual experiments are conducted to obtain the effective modulus under uni-axis loading and periodic boundary condition (PBC). Due to the merit of analytical integral in inhomogeneities, iBEM can handle with particle interactions and provide predictions of effective material behaviors. The effect of mesh refinement on the average field is investigated by adjusting the volume fraction, global size of the elements, which indicates with a comparatively coarse mesh could provide engineering applicable data. A many-particle system with $> 3,000$ particles are demonstrated for the convergence of the effective elasticity with the number of particles in the virtual material samples. In conclusions, this novel algorithm of iBEM for isotropic elastic composites with arbitrary polygonal/polyhedral inhomogeneities provides versatile capability to solve for both local fields and overall material behavior. It is a powerful tool for cross-scale modeling and virtual experiments of composites.

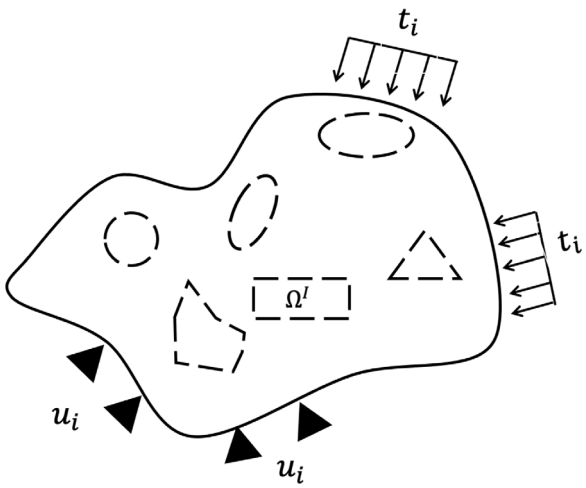

Fig. 1. Schematic illustration of multiple inhomogeneities embedded in a domain D with prescribed boundary conditions.

2. The formulation of the inclusion-based boundary element method (iBEM)

2.1. General problem statement

Consider multiple inhomogeneities Ω^I $(I = 1, 2, \ldots)$ embedded in a bounded domain D subjected to various boundary conditions shown as Fig. 1 such as Neumann, Dirichlet types. Shown in Fig. 1, the matrix domain is denoted by Ω^0 and therefore $D = \Omega^0 \bigcup_{I=1,2,\ldots} \Omega^I$. Notice that, for 2D problem, it can be an either plane stress or plane strain problem. This paper uses plane strain for the formulation in which the inhomogeneities can be considered as long prisms or fibers with the corresponding cross sections. However, the formulation can be used for plane stress problems by replacing the elastic moduli. Here t_i and u_i are prescribed tractions and displacements, respectively. An inelastic strain may exist on Ω^I, written as ε^{*I}_{ij}, which can, for example, be a thermal strain or misfit strain, and is also called eigenstrain [4]. For the isotropic elastic medium, let $C^I_{ijkl} = \lambda^I \delta_{ij}\delta_{kl} + \mu^I(\delta_{ik}\delta_{jl} + \delta_{il}\delta_{jk})$, where λ^I and μ^I denote the Lame constants of the Ith phase of the composite, where $I = 0$ and $I = 1, 2, \ldots$ representing the matrix and the Ith inhomogeneities phases, respectively. The governing equations can be written as,

$$C^I_{ijkl}(u_{k,li} - \varepsilon^{*I}_{kl,i}) + b_j = 0 \quad \text{for } \mathbf{x} \in \Omega^I \tag{1}$$

which is the Navier equation in each material domain of $I = 0, 1, 2, \ldots$. Here the displacement field u_k is continuous and differentiable whereas eigenstrain ε^{*I}_{kl} is piece-wise continuous. For simplicity, the body force b_j is taken as zero unless it is specified particularly.

Assuming no debonding on the interfaces, the boundary value problem of inhomogeneities could be enacted with the continuity equations of displacements and tractions in Eq. (2).

$$\sigma^+_{ij}(\mathbf{x})n^+_j = \sigma^-_{ij}(\mathbf{x})n^-_j, \quad u^+_i(\mathbf{x}) = u^-_i(\mathbf{x}) \quad \text{on } \partial\Omega^I \tag{2}$$

where $\partial\Omega^I$ represents the interface between the Ith subdomain and the matrix; superscript + and − denote the outer, inner surface of the interface, respectively; n_j is the unit normal vector of the surface.

Considering the traction and displacement boundary conditions on ∂D, this BVP could be solved by the multi-region BEM with two challenges: (1) the prescribed eigenstrain on the inhomogeneities needs to be addressed carefully; (2) the singularity on the vertices of polygon requires very fine elements to obtain an accurate results, which leads to high computational costs.

This paper proposes to avoid the multi-region BEM by using an eigenstrain to simulate the material mismatch. In our recent work [1,11,67], the inclusion problem (prescribed eigenstrain) and the inhomogeneity problem (equivalent inclusions) have been studied for elliptical/ellipsoidal particles, in which the displacement and strain/stress fields can be accurately predicted with a polynomial-form eigenstrain. For angular particles, since the Eshelby's tensor has singularities on the vertices (2D & 3D) and edges (3D), the eigenstrain distribution becomes complex in the neighborhood of them. Therefore, to address its complex distribution, a piece-wise function can be applied to approximate the eigenstrain with C^0 continuity. The governing equation in the absence of body force can be written as

$$(\lambda^0+\mu^0)u_{i,ij}+\mu^0 u_{j,ii}-C^0_{ijkl}\varepsilon^{*I}_{kl,i}=0 \tag{3}$$

where eigenstrain ε^{*I}_{kl} is piece-wise continuous on inclusions Ω^I $(I\neq 0)$ only and is zero on the matrix Ω^0. Compared with Eq. (1), Eq. (3) exhibits uniform stiffness over the whole domain D with eigenstrain sources on the inclusions Ω^I $(I\neq 0)$.

Using the Maxwell–Betti's reciprocal theorem with the aid of Green's function [33], one can write the solution with the Green's function technique:

$$\begin{aligned}u_i(\mathbf{x})=&\int_{\partial D}G_{ij}(\mathbf{x},\mathbf{x}')t_j(\mathbf{x}')d\mathbf{x}'-\int_{\partial D}T_{ij}(\mathbf{x},\mathbf{x}')u_j(\mathbf{x}')d\mathbf{x}'\\&-\int_D G_{ij}(\mathbf{x},\mathbf{x}')C^0_{mjkl}\varepsilon^*_{kl,m'}(\mathbf{x}')d\mathbf{x}'\end{aligned} \tag{4}$$

where $G_{ij}(\mathbf{x},\mathbf{x}')$ is the fundamental solution or elastic Green's function to describe the field at $\mathbf{x}$ caused by a point source field at $\mathbf{x}'$, which is written as in terms of the harmonic and bi-harmonic potentials as

$$G_{ij}(\mathbf{x},\mathbf{x}')=\frac{1}{4\pi\mu^0}\delta_{ij}\phi-\frac{1}{16\pi\mu^0(1-\nu^0)}\,\psi_{,ij} \tag{5}$$

and $T_{ij}(\mathbf{x},\mathbf{x}')=\frac{1}{2}C^0_{imkl}(G_{kj,l}+G_{lj,k})n_m$ is the fundamental solution of traction. The harmonic and bi-harmonic potentials can be written as $\phi=-\ln|\mathbf{x}-\mathbf{x}'|^2$ and $\psi=-|\mathbf{x}-\mathbf{x}'|^2\frac{\ln|\mathbf{x}-\mathbf{x}'|^2-1}{2}$ for 2D case [26], and $\phi=\frac{1}{|\mathbf{x}-\mathbf{x}'|}$ and $\psi=|\mathbf{x}-\mathbf{x}'|$ for 3D case, respectively.

In this paper, the closed-form domain integral of shape function interpolated eigenstrain is implemented in the iBEM code, which is elaborated in Appendix A and can be applicable to both the inclusion and inhomogeneity problems. Although we only demonstrate the domain discretization scheme with 6 - node triangular element (2D) and 10 - node tetrahedral element (3D), readers can follow the same fashion to extend for linear elements and other quadratic elements. Subsequently, the stress equivalent equations are setting up over the particle domain to transfer the inhomogeneity problem to an equivalent inclusion problem as follows [2,4]:

$$C^0_{ijkl}:(\varepsilon^b_{kl}+\varepsilon'_{kl}-\varepsilon^*_{kl})=C^I_{ijkl}:(\varepsilon^b_{kl}+\varepsilon'_{kl}) \tag{6}$$

where ε^b_{kl} is the strain caused by the boundary integral as follows:

$$\begin{aligned}\varepsilon^b_{kl}(\mathbf{x})=&\frac{1}{2}\int_{\partial D}[G_{kj,l}(\mathbf{x},\mathbf{x}')+G_{lj,k}(\mathbf{x},\mathbf{x}')]t_j(\mathbf{x}')\\&-[T_{kj,l}(\mathbf{x},\mathbf{x}')+T_{lj,k}(\mathbf{x},\mathbf{x}')]u_j(\mathbf{x}')d\mathbf{x}'\end{aligned} \tag{7}$$

and ε'_{kl} the strain caused by the area integral as follows:

$$\varepsilon'_{kl}(\mathbf{x})=-\frac{1}{2}\int_{\Omega}[G_{ki,jl}(\mathbf{x},\mathbf{x}')+G_{li,jk}(\mathbf{x},\mathbf{x}')]C^0_{ijmn}\varepsilon^*_{mn}(\mathbf{x}')d\mathbf{x}' \tag{8}$$

Given a polynomial eigenstrain distribution in an elliptical/ellipsoidal particle, the integral can be conducted analytically and the stress equivalence can be established in Appendix B. For angular particles, domain discretization will be introduced in the next section. Therefore combining the stress equivalent equations with the boundary element collocation, the eigenstrain and boundary displacement/traction can be solved and the overall elastic field can be calculated.

2.2. Closed-form domain integral with shape functions

The domain integral over the particle is obtained by the summation of the integrals over all elements through Eq. (4). Before considering the elastic fields caused by multiple elements/inhomogeneities, the integral of a single element on Ω^e is introduced as below and the entire solution is the superposition of all elements. Although the isotropic elastic Green's function differs in 2D and 3D problem, the domain integral for 2D can be derived in 3D Green's function by applying the Hadamard's regularization [8,26]. Therefore, for a uniform eigenstrain on an inclusion, the domain integrals in both 2D and 3D problems can be defined in terms of biharmonic Ψ and harmonic Φ potentials as Eq. (9).

$$\Psi=\int_{\Omega^e}\psi d\mathbf{x}',\quad \Phi=\int_{\Omega^e}\phi d\mathbf{x}' \tag{9}$$

And the domain integral of Green's function is obtained in terms of the two potentials as below,

$$\begin{aligned}g_{ikl}=&\int_{\omega^e}-G_{im,n}C^0_{mnkl}d\mathbf{x}'=\frac{1}{8\pi(1-\nu)}\\&\times\left[\Psi_{,ikl}-2\nu\Phi_{,i}\delta_{kl}-(1-\nu)(\Phi_{,k}\delta il+\Phi_{,l}\delta_{ik})\right]\end{aligned} \tag{10a}$$

$$\begin{aligned}S_{ijkl}=&\frac{1}{2}(g_{ikl,j}+g_{jkl,i})=\frac{1}{8\pi(1-\nu)}\\&\times\left[\Psi_{,klij}-2\nu\Phi_{,ij}\delta_{kl}-(1-\nu)(\Phi_{,ik}\delta_{jl}+\Phi_{,il}\delta_{jk}+\Phi_{,jk}\delta_{il}+\Phi_{,jl}\delta_{ik})\right]\end{aligned} \tag{10b}$$

where g_{ikl} and S_{ijkl} are Eshelby's tensors for displacement and strain, respectively. For linear or quadratic eigenstrain distribution, we can obtain the Eshelby's tensor similarly [26,27]. Following we use 2D problem as an example to demonstrate the domain discretization of eigenstrain distribution. Consider an arbitrary polygonal subdomain Ω^I, discretize it with E^I elements and N^I nodes, and the unknowns are eigenstrain on each node. Therefore, like other discretization methods, the eigenstrain inside the subdomain is piece-wise continuous. Without the loss of any generality, consider the 6 - node quadratic triangular element, say (x^1_1,x^1_2), (x^2_1,x^2_2), and (x^3_1,x^3_2) are the corner nodes, the eigenstrain distribution in the element can be written in terms of eigenstrain on the nodes as

$$\varepsilon^{*I}_{ij}(\mathbf{x}')=\sum_{n=1}^{3}(\varepsilon^{I*}_{ij})^n 2(L^n-1)L^n+\sum_{n=4}^{6}(\varepsilon^n_{ij})4L^IL^J \tag{11}$$

where $L^n=\alpha^n+\beta^n x_1+\gamma^n x_2$ is the area coordinates of the triangular element; α^I,β^I and γ^I are the components of shape functions of the Ith local node as (let the other two other local nodes be named as J,K, respectively),

$$\begin{aligned}&\alpha^I=\frac{x^J_1x^K_2-x^K_1x^J_2}{2A},\quad \beta^I=\frac{x^J_2-x^K_2}{2A},\quad \gamma^I=\frac{x^K_1-x^J_1}{2A},\\&2A=det\begin{bmatrix}1&x^1_1&x^1_2\\1&x^2_1&x^2_2\\1&x^3_1&x^3_2\end{bmatrix}\end{aligned} \tag{12}$$

In Eq. (11), the eigenstrain of an interior point is obtained through quadratic interpolation of the shape functions. Obviously, for both corner and middle points, the interpolation functions contains uniform, linear and quadratic components, thus one could rewrite the integral in superposition as Eq. (14),

$$\Lambda^I=\int_{\omega^e}L^I|\mathbf{x}-\mathbf{x}'|^2\frac{\ln|\mathbf{x}-\mathbf{x}'|^2-1}{2}d\mathbf{x}'=\alpha^I\Psi+\beta^I\Psi_1+\gamma^I\Psi_2 \tag{13}$$

$$\begin{aligned}\Lambda^{IJ}=&\int_{\omega^e}L^IL^J|\mathbf{x}-\mathbf{x}'|^2\frac{\ln|\mathbf{x}-\mathbf{x}'|^2-1}{2}d\mathbf{x}'=\alpha^I\alpha^J\Psi+(\alpha^I\beta^J+\alpha^J\beta^I)\Psi_1\\&+(\alpha^I\gamma^J+\alpha^J\gamma^I)\Psi_2+(\beta^I\gamma^J+\beta^J\gamma^I)\Psi_{12}+\beta^I\beta^J\Psi_{11}+\gamma^I\gamma^J\Psi_{22}\end{aligned} \tag{14}$$

where Ψ,Ψ_i and Ψ_{ij} are uniform, linear and quadratic biharmonic potentials defined in our recent work [26]. Notice for the displacement,

which is related to the third order partial derivative of the domain integral, requires the original form Φ_p. Since no partial differentiation is applied on Φ_p, the divergence theorem cannot be used, hence, in Appendix C, its original form is given for both 2D and 3D. Similarly, the shape function interpolated harmonic potentials could be expressed by Γ^I and Γ^{IJ} through changing the integral components as $\ln|\mathbf{x}-\mathbf{x}'|^2$. Then, using the technique of Green's function, the disturbed displacement field $u_i'(\mathbf{x})$ caused by eigenstrain in Ω^I is analytically formulated as Eq. (15),

$$-\int_{\Omega^I} G_{ij,m}(\mathbf{x},\mathbf{x}')C^0_{mjkl}\varepsilon^*_{kl}(\mathbf{x}')d\mathbf{x}' = \frac{1}{8\pi(1-\nu)} \times \left[\mathcal{A}_{kl,kli} - 2\nu\mathcal{B}_{kk,i} - 4(1-\nu)\mathcal{B}_{ik,k}\right] \tag{15}$$

where $\mathcal{A}_{ij}$ and $\mathcal{B}_{ij}$ are given as

$$\mathcal{A}_{ij} = \sum_{w=1}^{E^I}\sum_{n=1}^{4}(2\Lambda^{II}-\Lambda^I)(\varepsilon^*_{ij})^n - \sum_{n=5}^{10}4\Lambda^{IJ}(\varepsilon^*_{ij})^n \tag{16a}$$

$$\mathcal{B}_{ij} = \sum_{w=1}^{E^I}\sum_{n=1}^{4}(2\Gamma^{II}-\Gamma^I)(\varepsilon^*_{ij})^n - \sum_{n=5}^{10}4\Gamma^{IJ}(\varepsilon^*_{ij})^n \tag{16b}$$

Notice that in FEM, it interpolates the displacement with shape function, so the strain/stress inside one element maintains the continuity one order lower than the displacement; whereas the iBEM interpolates the eigenstrain instead and the analytical domain integrals of eigenstrain is always continuous and differentiable. For the 3D problem, the 10-node quadratic tetrahedral element is illustrated in [27] and elaborated in Appendix C.

Moreover, to demonstrate the method, we used the 6-node triangular and 10-node tetrahedral quadratic elements, which could map most of geometries of subdomains. However, it can be extended to other types elements, for example, the 3-node triangular or 4-node quadrilateral elements in 2D problem, 4-node tetrahedral and 8-node brick elements. Since the elastic fields is solved by domain integrals as Eq. (15), one only needs to modify the shape functions in Eq. (14) and Eq. (C.3), respectively. Taking 3-node triangular element as example, the shape functions contains the linear components, which can be handled completely in [26,27]. As for 4-node quadrilateral element, one needs to rewrite the shape function in terms of source, i.e $x_1^I x_2^I$, then those components can be integrated with linear and quadratic potentials. Following the same fashion, other types of elements can be applied directly. Although higher order elements, say cubic order of eigenstrain, might provide sound improvement in both mesh quality and convergence, the quadratic elements perform well with a few more elements as shown in the following case studies, so that we have implemented the algorithm up to quadratic shape functions in the iBEM code so far.

2.3. Equivalent stress conditions and the singularities of Eshelby's tensor and eigenstrain

For the cases of elliptical/ellipsoidal inhomogeneities, the eigenstrain is assumed as the Taylor series expanded at the centroid, hence, 18 and 60 equations are required for 2D and 3D problem, respectively [1] considering the symmetry of eigenstrain.

The domain discretization method proposed in Section 2.2 is a subdomain collocation method with the stress equivalent equations established on the subdomain and the unknowns are the eigenstrain of the nodes. Therefore, for each node, 3 and 6 stress equivalent equations are required, respectively. If one can establish the same number of linearly independent equations, the eigenstrain field can be solved and then the elastic field can be illustrated. A natural way to establish the equation system is to set up stress equivalence on all the nodes themselves. However, due to the singularity at the vertices and discontinuity of Eshelby's tensor on the edge (2D) or surface (3D) points, the numerical issue should be well addressed to obtain practical solutions.

In the conventional boundary element method (BEM), for the multi-region initial strain/stress problem, the equations setting up at the interfaces are on the displacements and tractions, which is one-order lower singularity compared to the strain field. In the literature, the strain/stress fields on the interfaces are recovered by multiplying the displacement [68], traction with the derivative form of shape functions, which is similar to FEM. Other researchers [30,69] mapped the linear 3-node linear triangular element and 4-node linear tetrahedral element into isoparametric square, cubic coordinates, respectively. Although using the mapping coordinates could approximately solve the 2D problems, it downgrades the merit of analytical domain integrals of the Eshelby's tensor and is challenging to be extended to 3D problems. Therefore, in this paper, an alternative scheme is proposed to set up the stress equivalent equations on the Gauss integral points instead of exactly on the nodes themselves, which avoids the singularity issue, as follows:

(1) For the Ith element, derive the stress residual on each Gauss integral point from the stress equivalent condition in Eq. (17),

$$(\sigma^d)^I = \Delta C_{ijkl} : (\varepsilon^b_{kl} + \varepsilon'_{kl}) + C^0_{ijkl} : \epsilon^*_{kl} \tag{17}$$

where $\Delta C_{ijkl} = C^I_{ijkl} - C^0_{ijkl}$ is the mismatch of stiffness tensor. Since the original stress equivalent equation is expected to hold at any point of the inhomogeneity, thus, a necessary or weaker condition is the stress residual over the Ith element is zero.

(2) Apply the weight of each Gauss point on its stress residual σ^d and distribute it on the nodes of the element. For simplicity, this paper uses the same number of Gauss points as the nodes in the element and assign the residual to the closest node. However, more Gauss points can be used and other distribution method can be used.

(3) Collect the weighted stress residuals on each node and make the sum equal to zero. If one node only exhibits on one element, no summation is necessary. Otherwise, the contribution from each element should be considered.

Therefore, we can set up the closed system of linear equations. Notice that Steps (2) and (3) can be implemented by the collection of stress residuals on a node by integrating the weighted residual on the neighboring Gauss points with the aid of a kernel function. However when a node is associated with only one element or Gauss point, the integral weight on the stress residual on a vertex node is trivial.

When the linear equation system for eigenstrains and boundary unknowns is established and solved, one can use them to calculate the displacement field by the area integral in Eq. (4). Therefore, the strain and stress fields can be calculated. Notice that as shown in Appendix D, the Eshelby's tensor exhibits a $\ln r$ singularity on vertices [20,26] for 2D problems as well as $1/r$ on vertices and $\ln r$ on edges for 3D problems [20,27]. As a result, the eigenstrain on the vertex also exhibits a singularity of $\ln r$ and $1/r$ for 2D and 3D problems, respectively. Therefore, the stress singularity in the inhomogeneity problem may end up at $\ln^2 r$ and $1/r^2$ for 2D and 3D problems, respectively. Although the particle discretization exhibits numerical errors with a shape function of eigenstrain distribution, because eigenstrain is indeed continuous within the particle, the influence zone of the singularity on the vertices is small (Appendix D), and also the area integral is based on the exact solution, this algorithm can provide high-fidelity results to the elastic field with low mesh sensitivity. In addition to the physical singularities on the vertices and along the edges, the handling of mathematical singularities at the interior nodes (i.e., post process to solve stress / strain) is also elaborated in Appendix D.

2.4. Implementation of the iBEM algorithm

The formulation of iBEM has been implemented with the C++ code. The iBEM has successfully simulated > 1000 ellipsoidal particles [1] or elliptical particles. The above stress equivalent equations

$$
\underset{(dim\times N^b+\frac{13}{2}(dim^2+dim)N^{ell}+\frac{dim^2+dim}{2}N^i)^2}{\begin{bmatrix} Q+H & \dots & -g^{0I} & -g^{1I} & -g^{2I} & \dots & -\mathcal{K}^J & \dots \\ \vdots & \vdots & \vdots & \vdots & \vdots & \vdots & \vdots & \vdots \\ \Delta C^I H^{1I} & \dots & \Delta C^I S^{0I} & \Delta C^I S^{1I} & \Delta C^I S^{2I} & \dots & \Delta C^I \mathcal{F}^J & \dots \\ \Delta C^I H^{2I} & \dots & \Delta C^I S^{0I'} & \Delta C^I S^{1I'} & \Delta C^I S^{2I'} & \dots & \Delta C^I (\mathcal{F}^J)' & \dots \\ \Delta C^I H^{3I} & \dots & \Delta C^I S^{0I''} & \Delta C^I S^{1I''} & \Delta C^I S^{2I''} & \dots & \Delta C^I (\mathcal{F}^J)'' & \dots \\ \vdots & \vdots & \vdots & \vdots & \vdots & \vdots & \vdots & \vdots \\ \Delta C^J H^{1J} & \dots & \Delta C^J S^{0J} & \Delta C^J S^{1J} & \Delta C^J S^{2J} & \dots & \Delta C^J \mathcal{F}^J & \dots \\ \vdots & \vdots & \vdots & \vdots & \vdots & \vdots & \vdots & \vdots \end{bmatrix}}
\underset{(dim\times N^b+\frac{13}{2}(dim^2+dim)N^{ell}+\frac{dim^2+dim}{2}N^i)}{\begin{bmatrix} u \\ \vdots \\ \varepsilon^{*0I} \\ \varepsilon^{*1I} \\ \varepsilon^{*2I} \\ \vdots \\ \varepsilon^{*J} \\ \vdots \end{bmatrix}}
= \underset{(dim\times N^b+\frac{13}{2}(dim^2+dim)N^{ell}+\frac{dim^2+dim}{2}N^i)\times(dim\times N^b)}{\begin{bmatrix} U \\ \vdots \\ -\Delta C^I U^{1I} \\ -\Delta C^I U^{2I} \\ -\Delta C^I U^{3I} \\ \vdots \\ -\Delta C^I U^{1J} \\ \vdots \end{bmatrix}}
\underset{(dim\times N^b)}{\begin{bmatrix} t \end{bmatrix}} \tag{18}
$$

Box I.

can be integrated into the global matrix Eq. (18) for the simulation of polyhedral/polygonal and ellipsoidal/elliptical particles in the bounded domain (see Box I), where $dim = 2 \text{ or } 3$ for the 2D or 3D problem, respectively; $\mathcal{Q}$ is diagonal matrix introduced by the rigid body method to eliminate the singularity issues of BEM [36] , which is elaborated in Appendix E ; $\mathcal{K}^J$ and $\mathcal{F}^J$ denote the summation of domain integrals of Green's function regarding to displacement and strain fields of the Jth node, respectively. The rank of the matrix is marked under itself. Again, N^b is number of boundary nodes; N^{ell} is the number of elliptical inhomogeneities; N^i is the total number of nodes of polygonal/polyhedral inhomogeneities.

Here the interactions between inhomogeneities and boundary are considered as follows:

(1) The interactions between inhomogeneities and boundary is introduced by the components, i.e g^{0I}, $\mathcal{K}^J$, where the superscripts I, J represent the Ith elliptical inhomogeneity and Jth polygonal internal node, respectively. The superscript $0, 1, 2$ denote the uniform, linear and quadratic terms with respect to the eigenstrains, as shown in Appendix B.

(2) The interactions between inhomogeneities is considered in stress equivalent equations inserted below the traditional BEM global matrix, where $'$ means the partial derives of the Eshelby's tensor. Eq. (18) considers the uniform, linear and quadratic eigenstrain terms, although lower order terms could predict the field accurately for some cases, such as dilute particle distributions and stiffer fibers.

Once the eigenstrain distribution is obtained, the displacement and strain/stress fields could be calculated. Unlike other methods with numerical integrals or approximation of the internal fields, the iBEM algorithm keeps the advantage of BEM that all the elastic fields could be expressed in the analytical form.

3. Numerical verification and comparisons with FEM

The aforementioned algorithm has been implemented in the software package to conduct virtual experiment with various boundary conditions. To verify its accuracy, this section conducts two numerical cases studies: (1) subdomain with prescribed eigenstrain, i.e, thermal strain; (2) inhomogeneity embedded matrix under a vertical uniform load. Shown in Fig. 2, the isosceles triangle (2D) / tetrahedral (3D) with edge and height $w = h = 0.1m$ are embedded in the matrix, whose bottom are fixed. The load is applied on the subdomain or the boundary. For the boundary element part, (1) 200 3-node line elements (2D); (2) 1,176 4-node quadrilateral elements (3D) are applied, while the domain discretization in the subdomains vary in cases. For the finite element part, the types of elements used are (1) combination of linear, quadratic triangular elements and bilinear quadrilateral elements (2D); (2) combination of linear, quadratic tetrahedral elements and trilinear hexahedral elements (3D).

3.1. Inclusion problem for a subdomain with prescribed eigenstrain

Firstly the inclusion problem is considered as the subdomain exhibits the same stiffness as the matrix. Structural steel is selected with Young's modulus $E_s = 200$ GPa, Poisson's ratio $\nu = 0.3$ and thermal expansion coefficient $\alpha_s = 1.2\times10^{-5}\frac{m}{m.^\circ C}$. When a triangular/tetrahedral sample is taken out, to repair the hole, a similar larger sample is cooled down ($C^I = C^0$) 20° to tightly refill it without welding. The misfit strain can be described by the thermal strain as well in form of a prescribed eigenstrain $\varepsilon^*_{ij} = 2.4\times10^{-4}\delta_{ij}$.

Due to the eigenstrain, the displacement/strain field around the neighborhood of the inclusion is disturbed. The elastic field can be analytically expressed with the integral of the inclusion domain and boundary integral as well. Hence, the domain discretization in iBEM is unnecessary and a single element produces the convergent results shown in Fig. 3,

However, the FEM requires many elements to illustrate the variation of the elastic field due to the singularity at the vertex. To illustrate the convergence situation of the FEM, the cases with three FEM meshes at the height of 1.25 (746 elements), 0.3125 (4128 elements) and 0.05 (178,436 elements) cm are applied for 2D problem; whereas the height of 1.25 (37,104 elements), 0.3125 (232,398 elements) and 0.1 ($1,418,222$ elements) cm are used for 3D problem. Notice that the size of elements is altered in the subdomain and its neighborhood accordingly to generate mesh with smooth transition. Indicated in Fig. 3, good agreement with the convergent results of FEM is observed with a single element for the inclusion problem of the iBEM, since it is the analytical domain integral of the Green's function.

Although overall the FEM could provide convergent results with refined mesh, it is observed that the numerical instability at the vertex, particularly for 3D case, because it exhibits higher singularity level of $1/r$ than the 2D case of $\ln r$ [20,26,27]. Because iBEM has included the singularity into the analytical integral of the Eshelby's tensor, it is robust and stable once the eigenstrain is prescribed.

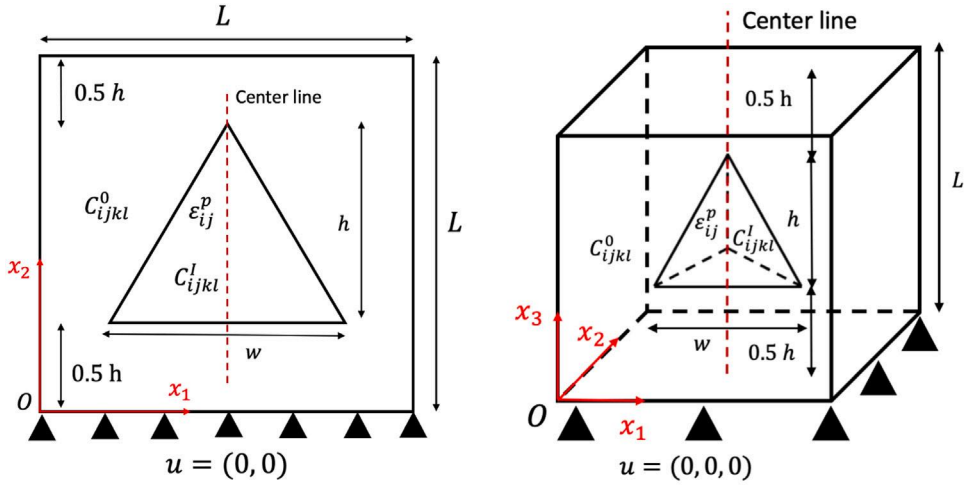

Fig. 2. Geometry and boundary conditions of the inclusion problem with a prescribed strain ε^p_{ij}.

Fig. 4 shows the comparison of converged stress distribution with stress concentration and singularity at the neighborhood of the vertices for the 2D case between iBEM and FEM. The number of elements used in iBEM are 201 (200 for boundary mesh and 1 for the triangular inclusion); while in FEM, 171,949 elements are applied for smooth stress plot (both inclusion and inhomogeneity case). Due to the boundary confinement at the bottom, the variation of stress field exhibits a gradation pattern in the x_2 direction with in the subdomain, and the variation at the vertices at the bottom is smaller than the top vertex. Comparing Fig. 4(a), (b) with Fig. 4(c) and (d), it is hard to identify the differences between them as the stress local fields are similar. However, there are some minor differences in the neighborhood of the vertices and the edges of the triangular subdomain. Notice that the stress contour plot (Fig. 4(a) and (b)) are plotted with uniformly distributed points, say 401×401, and there is no approximation as the stress is computed with analytical integral equations. As for FEM, if one uses the interpolated stress (stress at some point of the specific element), the results are approximated with numerical errors. To mitigate such effects, only the stress of the nodes are selected to plot, which is the reason why the edges of Fig. 4(c) and (d) are with less stress fluctuations.

3.2. Triangular/tetrahedral inhomogeneity under a uni-axial load

In this section, the subdomain in Section 3.1 is substituted with an aluminum alloy with Young's modulus $E_a = 70$ GPa and Poisson's ratio $\nu_a = 0.33$. In addition to the boundary conditions prescribed in Fig. 2, a downward uniform axis load 1 MPa is applied at the top line (2D) / surface (3D). Other sides are free of traction. Therefore, it becomes an inhomogeneity problem for the material mismatch between the particle and matrix. Herein the mismatched eigenstrain is used the simulate the material difference in the equivalent inclusion problem, and it varies in an angular particle. The domain discretization will be used and the results will be compared with the FEM results as Fig. 5. For the 2D triangular problem, 1, 4 and 25 elements are applied in the inhomogeneity. Interestingly, when a single element is used on the inclusion, though the solution exhibits a small disparity from the convergent FEM results (178,436 elements), it predicts the trend and singularity of elastic solutions pretty well, because the Eshelby's tensor of the particle plays the dominant role and the influence region of the eigenstrain singularity is quite limited, which is shown in Appendix D. When the number of elements increase, say 4, the difference between FEM and iBEM rapidly reduces and it agrees well even in the neighborhood of vertex. It is observed that a more refined mesh indeed improves the results, as the number of elements increase 25. However, the disparity between $iBEM-25$ and $iBEM-4$ is negligible, which implies the good convergence behavior. Similarly, for the 3D problem, 1, 8 and 64 elements are employed. Due to the higher order of singularities and discontinuity of the surfaces, the 8 element case has little discrepancy around the bottom part of the tetrahedron. The stress curve $iBEM-\sigma_{11}(8)$ is parabolic in $[0.05, 0.10]m$, exactly inside one element, which suggests a refined mesh will provide better stability. Hence, in the 64 element case, the solution agrees well with the convergent FEM results ($1,418,222$ elements). Moreover, for FEM, it is barely possible to describe stress singularities with such small number of elements, since a high number of nodes is necessary to shown the large variation of a curve with displacement on the nodes.

Fig. 6 shows the comparison of contour plot of the stress field between iBEM and FEM. The number of elements used for iBEM are 225 (200 for boundary mesh and 25 for triangular subdomain).In comparison with Fig. 4 for the inclusion problem, the stress in the inhomogeneity problem varies more intensively because eigenstrain is not uniform as the inclusion problem. As shown in Appendix D, because the eigenstrain may approach infinite or zero at the vertices, the stress singularity in the inhomogeneity problem can be at a higher level than the inclusion problem with a uniform eigenstrain.

3.3. Circular inhomogeneity under a uni-axial load

The iBEM can handle with the ellipsoidal particles by using the classical solution of Eshelby's problem [2,4] and the present boundary integral equations. As a demonstration, this section only applied the 2D case with a circular inhomogeneity [26], and the ellipsoidal cases are elaborated in our recent work [1,11,67]. Considering a circular aluminum alloy ($E_a = 70$ GPa, $\nu_a = 0.33$) inhomogeneity with diameter $a = 10$ cm is placed at the center of a 20×20 cm^2 square steel plate. Thanks to the analytical domain integral [1,4], no mesh is needed for the circular inhomogeneity but the polynomial form of eigenstrain can provide tailorable accurate results. Here the stress field from the iBEM is compared with FEM of at 3 cases with uniform, linear and quadratic eigenstrains, respectively.

Notice that this is different from the classic Eshelby's inhomogeneity problem because the finite domain is used. Specifically, the boundary integral plays a role on the eigenstrain distribution in the EIM. If the domain size increases, the linear or quadratic eigenstrain terms will reduce and the constant eigenstrain can reach high accuracy as Eshelby's solution does.

Indicated in Fig. 7, there exists no singularity effect in the local field and the difference between "quadratic" term and FEM is very

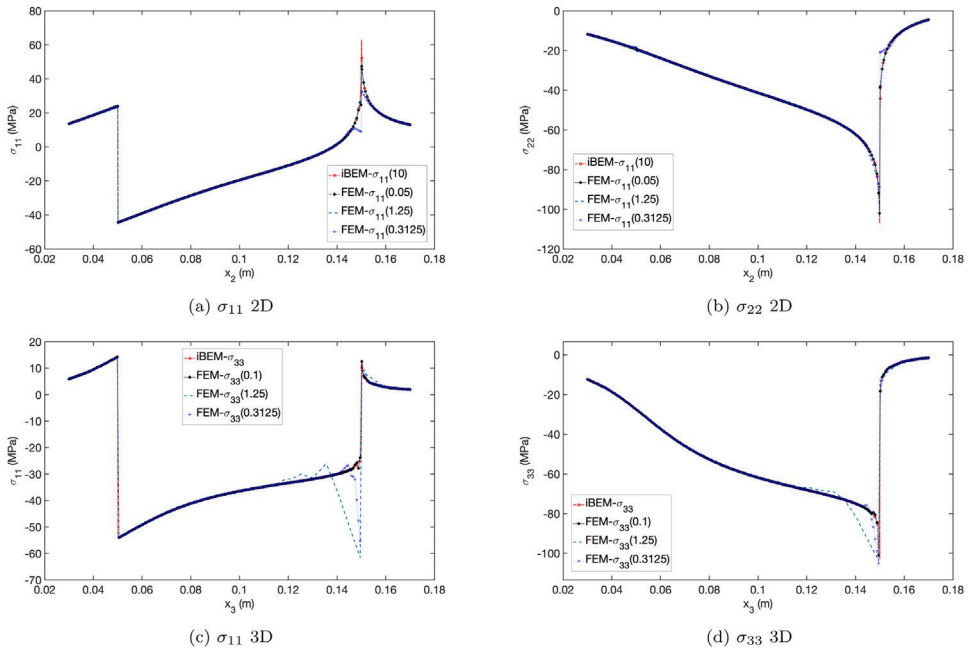

(a) σ_{11} 2D (b) σ_{22} 2D

(c) σ_{11} 3D (d) σ_{33} 3D

Fig. 3. Comparison of the stress distribution (a)σ_{11} (b) σ_{22} (2D); (c) σ_{11} (d) σ_{33} (3D) along the x_2 and x_3 for 2D and 3D, respectively, in the range of $[3, 17]$ cm between FEM and iBEM on inclusion problem with the prescribed eigenstrain $\epsilon^p_{ij} = 2.4 \times 10^{-4}\delta_{ij}$.

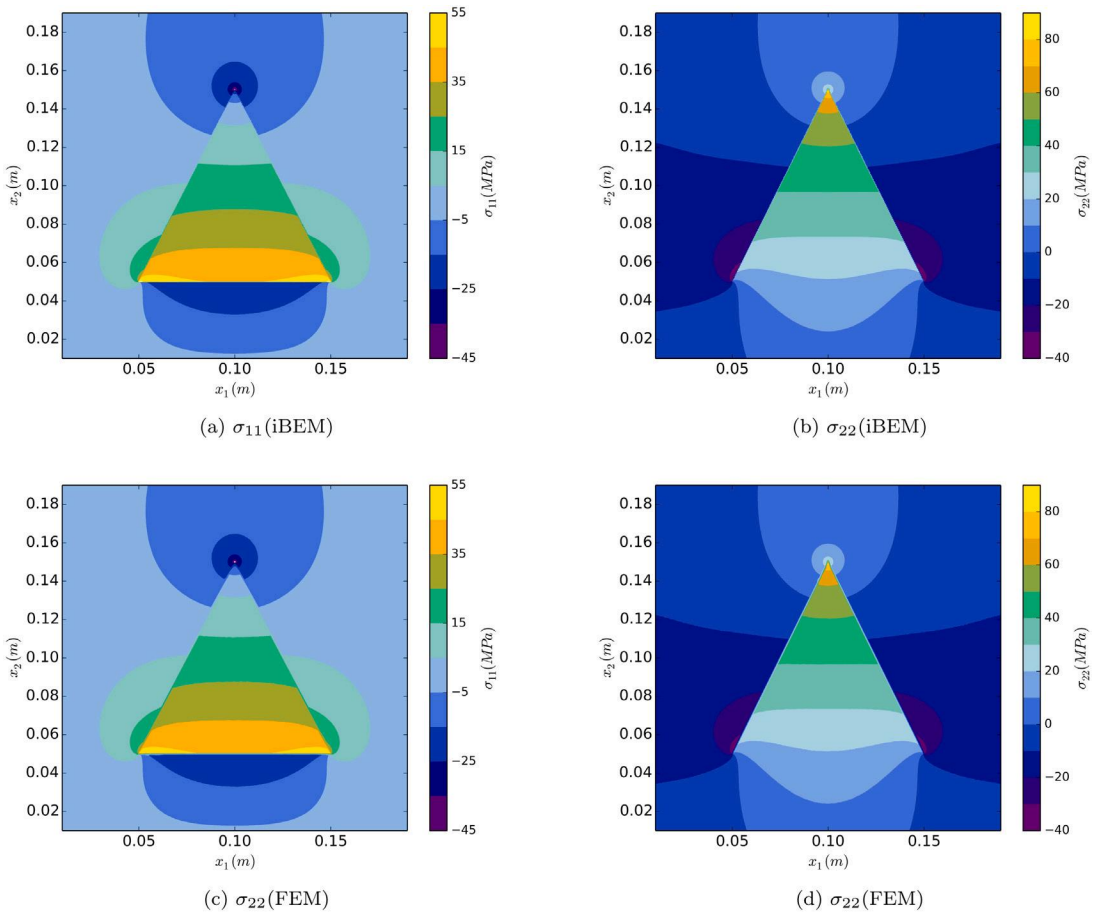

(a) σ_{11}(iBEM) (b) σ_{22}(iBEM)

(c) σ_{22}(FEM) (d) σ_{22}(FEM)

Fig. 4. Comparison of contour plot of the normal stresses field in the square of the range $x_1 \in [1, 19]$ cm and $x_2 \in [1, 19]$ cm for the inclusion problem with prescribed eigenstrain for the 2D problem.

small. Notice that even only one inhomogeneity is considered, the "uniform" and "linear" terms of eigenstrain may not capture the change of eigenstrain field as the particle and the matrix are at the similar dimension, which leads to inaccurate approximation of the stress field.

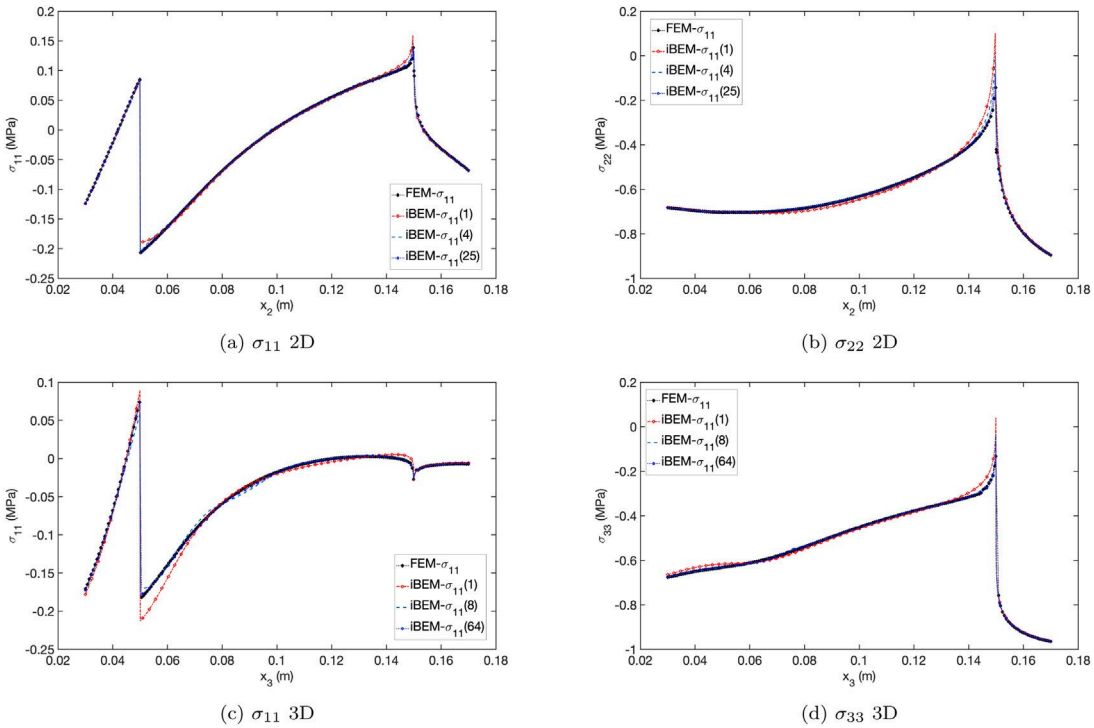

Fig. 5. Comparison of the normal stress distribution (a)σ_{11} (b) σ_{22} (2D); (c) σ_{11} (d) σ_{33} (3D) along the x_2 and x_3 for 2D and 3D, respectively, in the range of $[3, 17]$ cm between FEM and iBEM on inhomogeneity problem with a uniform boundary pressure on the top line/surface of the square/cube.

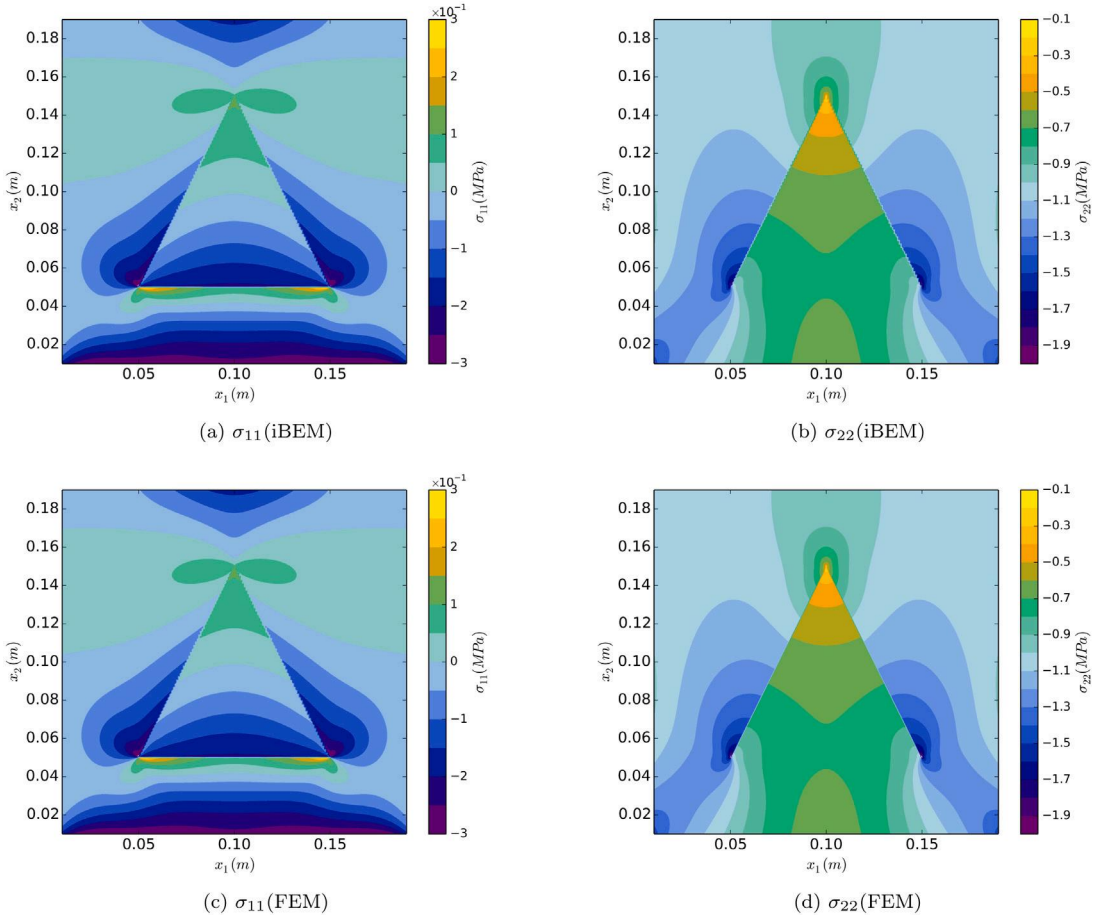

Fig. 6. Comparison of contour plot of the normal stresses field in the square of the range $x_1 \in [1, 19]$ cm and $x_2 \in [1, 19]$ cm for the 2D inhomogeneity problem under a uni-axial load.

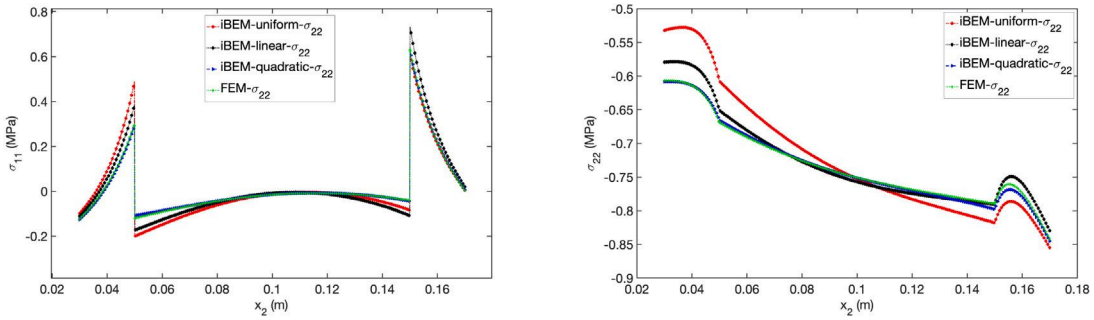

Fig. 7. Comparison of the stress distribution (a) σ_{11} and (b) σ_{22} along x_2 between FEM and iBEM (3 levels of accuracy) for the circular inhomogeneity problem.

With the quadratic term, iBEM provides excellent agreement with the FEM which uses 40,900 small elements at a size of 0.1 cm. Surely, the isogeometric analysis (IGA) with FEM might avoid the problem of geometric approximation and reach high accuracy with less elements. It is in another category of consideration as IGA can be applicable to iBEM as well.

Different from angular inhomogeneity, although the stress discontinuity exists cross the boundary of the sub-domain, the traction and displacement continuity is still satisfied, and no stress singularity is induced. Although the higher order of eigenstrain provides more accurate results, the shape of stress distribution curve for the uniform eigenstrain is similar to those for the linear or quadratic eigenstrain distribution, because the Eshelby tensor for the constant eigenstrain plays a dominant role on the domain integral.

4. Results and discussion

This section will use the iBEM to solve inhomogeneity problems and demonstrate its unique capability to simulate heterogeneous material systems. Although both 2D and 3D cases are implemented in the iBEM, this section mainly uses 2D cases to illustrate the method unless it is specified for 3D cases. However, most conclusions in 2D cases can be generalized to 3D cases as well.

4.1. Mesh choice of polygonal inhomogeneities

Discussed in Section 3.2, there exists singular effect of stresses in the neighborhood of the vertices, where the eigenstrain exhibits a larger variation in comparison to the eigenstrain field of the central part. In this section, the contour plots of eigenstrain field with 3 different global element size are applied below as, (1) 5 cm (4 elements); (2) 2 cm (25 elements); and (3) 0.5 cm (426 elements). Shown in Fig. 8, each contour plot contains 24 levels to exhibit the difference. The ε^*_{22} is concentrated around the middle part, whereas ε^*_{11} concentrates around the two side vertices. Although the overall distribution follows the similar pattern for three element resolutions, obviously smaller elements can capture the eigenstrain singularity better with a larger distribution range. Refiner mesh does not improve much in the middle parts, because the singularity effect is limited to the neighborhood of the vertices. The peak eigenstrain is located at the top area along the edges, where the dark red area ($\varepsilon^*_{22} > 2.7 \times 10^{-6}$) reduces as the global elements decreases.

The above observations provide an alternative mesh strategy to improve both the accuracy and efficiency that: (1) for interior middle part, one could simply use larger/coarse mesh; (2) extra attentions could be paid on the neighborhood of the vertex and edges, if one pursues the high accuracy. Notice that because Eshelby's tensor is size independent, iBEM can maintain good numerical stability even with very fine elements. However, in the comparison with FEM in Fig. 5, 4 and 25 elements cases have already predicted accurate results, which implies that the change of eigenstrain at some "sensitive" regions (i.e, around vertices or edges) only produces limited influences to the global solutions. In the common sense, no special measurements are required to be applied at those regions during the mesh process, a uniform mesh is acceptable.

Notice that as shown in Appendix D, because the elastic field is obtained by the integral of eigenstrain over the particle domain and the influence of the eigenstrain at one point decays at $1/r^2$ or $1/r^3$ for 2D or 3D problems respectively, a minor error at one point may not affect the overall accuracy significantly. Particularly, although the eigenstrains at the vertex and boundary nodes are sensitive to the mesh, their effects on overall results of the stress distribution are localized on their neighborhood. That is the reason why even a single element can provide good prediction of the trend of elastic field variation.

4.2. Inhomogeneity-boundary interactions

Shown in Fig. 2, the triangular inhomogeneity is located at the center of the square along the x_2 axis, where the distance between the bottom line and boundary is 5 cm. In order to observe the boundary effect, the distances are modified as $0.5, 2, 4, 6$ cm, respectively. In Fig. 9(a), the variation of normal stresses are compared along the x_2 direction in the range of $[0.1, 17]$ cm. The stress discontinuity exists at the bottom for σ_{11} only while σ_{22} remains continuous, whereas the singularity is observed for both stresses at the top vertex. When the inhomogeneity moves toward the center, stress discontinuity at the bottom difference grows, because the boundary confinement reduces.

The other example in this section investigate the effect of the dimension of the triangles, say $w = h = 2, 5, 10$ and 18 cm. Shown in Fig. 10, the variation of normal stresses are compared along the x_2 axis, when $d = 0.5$ cm. With the increase of the triangle size, the boundary confinement reduces the levels of stress discontinuity and singularity. It provides some insight that grain boundary could strengthen materials although the interfacial strength can be an issue.

4.3. Interactions between inhomogeneities

In the previous section, the boundary effect on the stress field is significant if the inhomogeneity is close to the boundary. Besides the boundary interactions, another important issue is inhomogeneity interactions, especially when they are close to each other. Without changing the matrix geometry shown in Fig. 2, inhomogeneities are rearranged as shown in Fig. 11 as top-down (2 triangular inhomogeneities), side by side (2 triangular inhomogeneities). The material assignment keeps the same as previous sections, but one case study is added by switching the material properties of matrix and inhomogeneities. Since the interactions between inhomogeneities are dependent on the ratio of the distance to the width w of inhomogeneity, therefore, the ratio is set as 0.05 for an intensive interaction. In addition, the boundary effect is also included by setting the exactly same distance $d = 0.5$ cm. The dimensions of the triangles are modified as $h = 9.25$ cm and $w = 10$ cm to satisfy the above conditions.

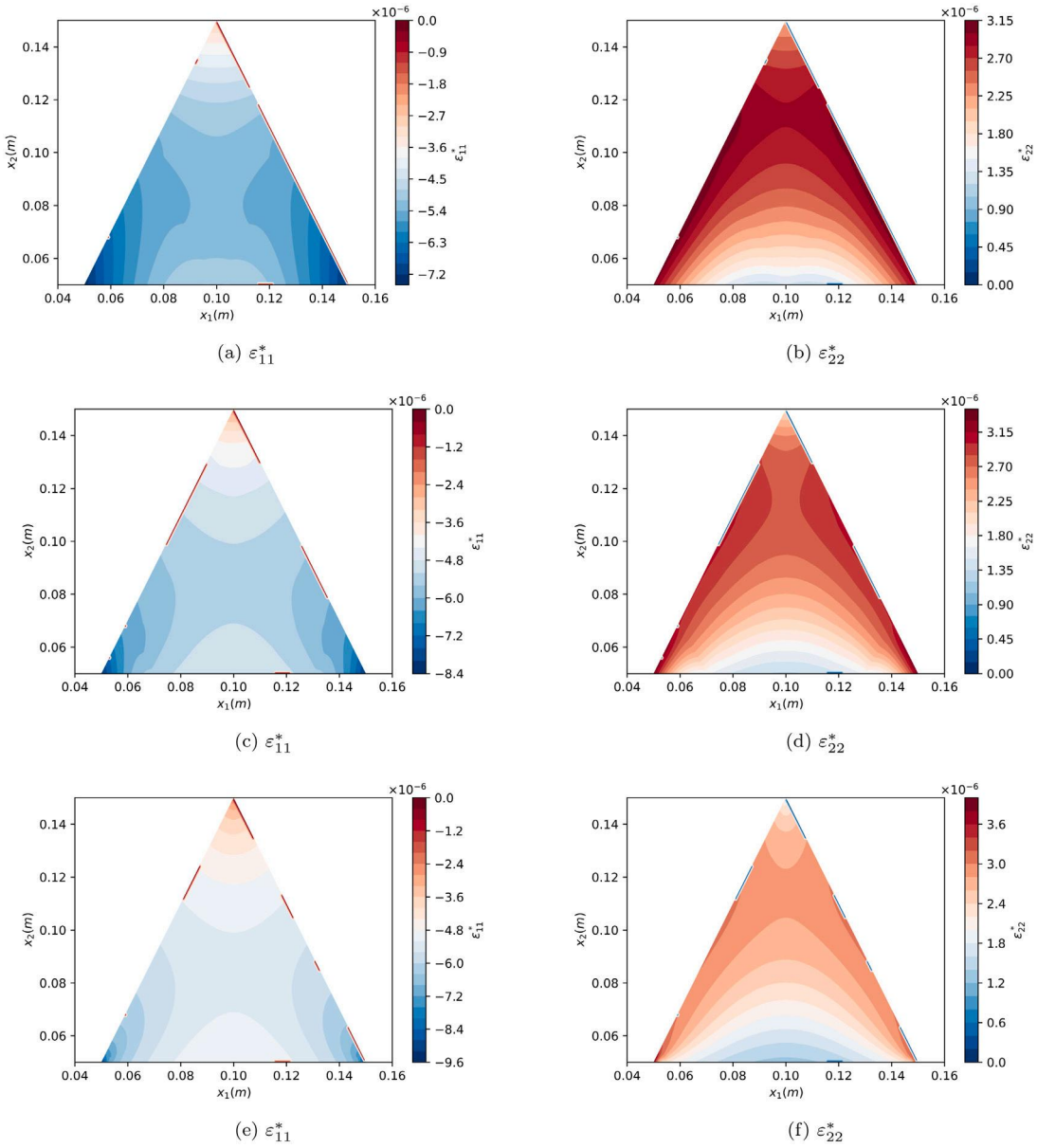

Fig. 8. Contour plot of the eigenstrain over the triangular inhomogeneity domain under the uni-axial downward pressure 1 MPa. (a) eigenstrain ε^*_{11} and (b) ε^*_{22} with global element size 5 cm; (c) eigenstrain ε^*_{11} and (d) ε^*_{22} with global element size 2 cm; (e) eigenstrain ε^*_{11} and (f) ε^*_{22} with global element size 0.5 cm.

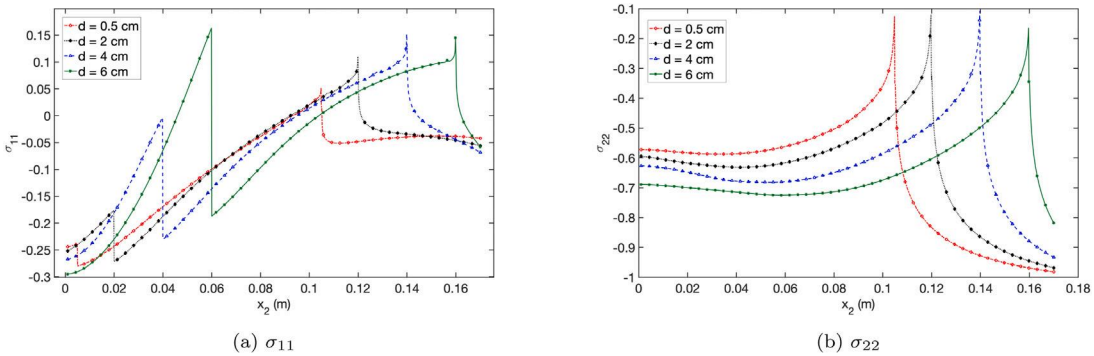

Fig. 9. Normal stresses variation along the x_2 axis in range of $[0.1, 17]$ cm with different particle locations, whose distances to the bottom boundary are $0.5, 2, 4, 6$ cm.

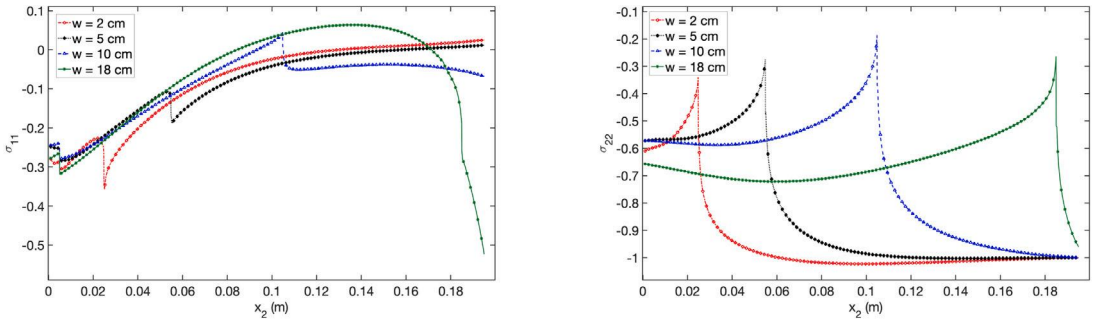

(a) σ_{11} (b) σ_{22}

Fig. 10. Normal stresses variation along the x_2 axis in range of $[0.1, 19.5]$ cm with different particle sizes, whose width are $2, 5, 10$ and 18 cm.

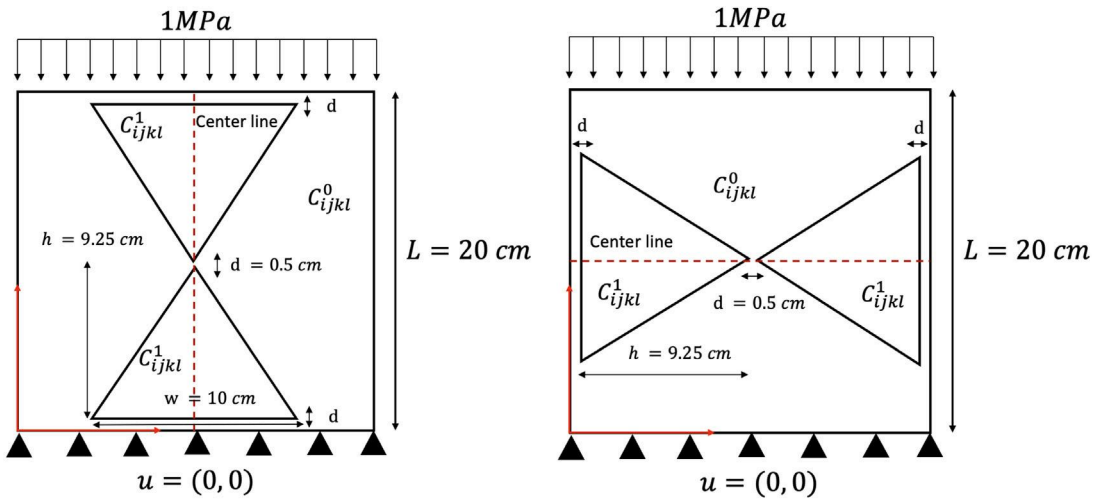

Fig. 11. Schematic plot of the placements and boundary conditions of the two triangular inhomogeneities, (a) top-down; (b) side by side.

4.3.1. *Top-down inhomogeneity interaction*

Shown in Fig. 12, the normal stresses distribution along the x_2 (symmetric center line) is plotted for both stiff and soft inhomogeneity cases by switching steel and aluminum for the inhomogeneity and matrix, respectively. When aluminum is particle, the stress on the particles changes small due to the boundary confinement. However, when steel is particle, the stress increases significantly in the loading direction.

4.3.2. *Side-by-side inhomogeneity interaction*

Shown in Fig. 13, the normal stresses distribution along the x_1 (symmetric center line) is plotted for both stiff and soft inhomogeneity cases for the side-by-side particle interaction. The stress distribution on the particles exhibit opposite trends between stiff and soft particle cases. Stress is relaxed slightly between the two vertices. Although a compressive uni-axial load is applied along x_2 direction, significant tension is induced in x_1 direction for stiff particle case when particles are close to each other.

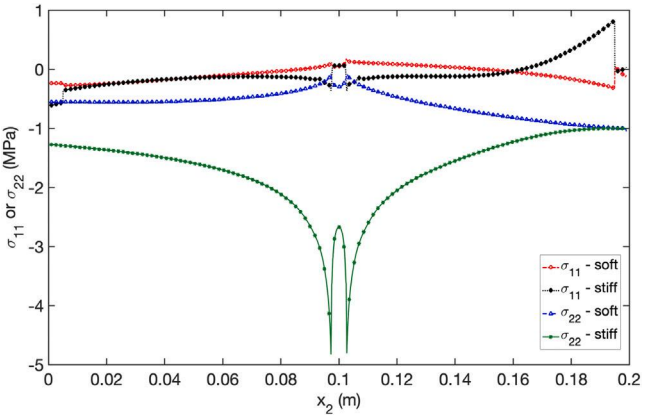

Fig. 12. Normal stresses variation along x_2 axis in range of $[0.1, 19.9]$ cm with top-down inhomogeneity interactions.

4.3.3. *Top-down circular and triangular inhomogeneities interaction*

In this section, the top triangle is replaced by a circular inhomogeneity with radius $a = 3$ cm as shown in Fig. 14. The normal stresses distribution along the x_2 (symmetric center line) is plotted for both stiff and soft inhomogeneity cases in Fig. 15. Stress σ_{22} exhibits singularity still at the vertex of the triangle but no singularity at the circle boundary. Although stress discontinuity exists, it is a small gap compared with the singularity. Compared with Fig. 12, the circular particle case exhibits lower stress variation for both stiff or soft particle cases. Therefore, if possible, angular inhomogeneities shall be avoided for minimizing the local stress variation.

Fig. 16 illustrates the detailed stress distribution. Around the circular inhomogeneity, stress concentration of σ_{22} occurs at two sides of the aluminum particle in compression; while tensile stress of σ_{11} is

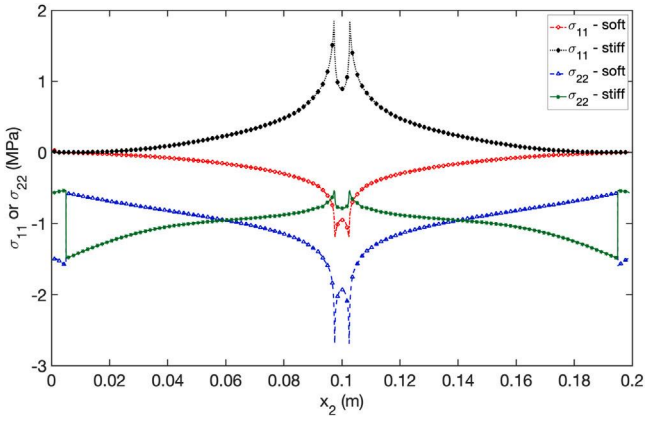

Fig. 13. Normal stresses variation along x_1 axis in range of $[0.1, 19.9]$ cm with side-by-side inhomogeneity interactions.

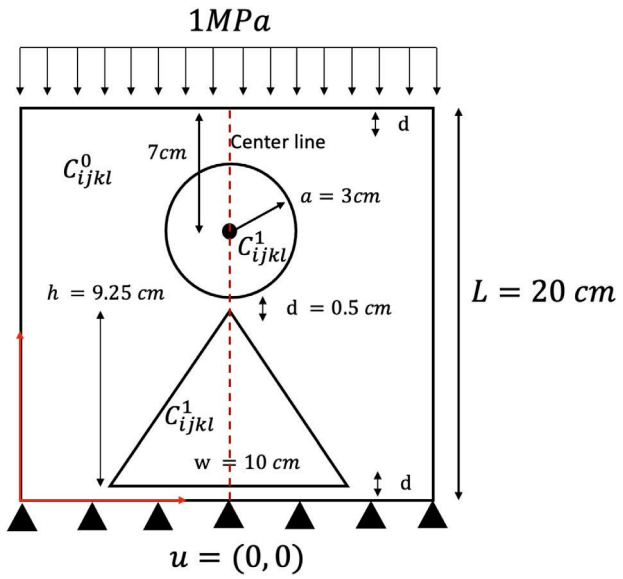

Fig. 14. Schematic plot of the placements and boundary conditions of the one triangular and one circular inhomogeneities.

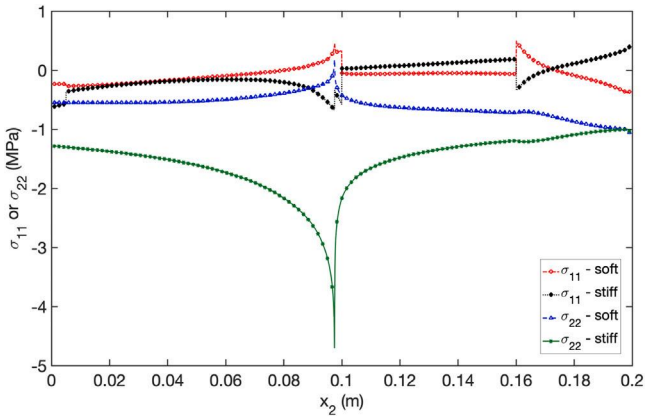

Fig. 15. Normal stresses variation along x_1 axis in range of $[0.1, 19.9]$ cm with top-down circular and triangular inhomogeneity interactions.

induced on its top and bottom. For the case of the circular steel particle, the stress level on the particle is much higher than the aluminum case due to the stiffer particle. Around the triangular inhomogeneity, the stress variation mainly occurs around the neighborhood of the vertex and is relatively small in the other range, which also confirms that the eigenstrain is more uniform, so that coarse mesh may provide a reliable result. Particularly, because the singularities are localized at the vertices, the effect to the overall material behavior may be averaged out, which will be discussed in the following section.

As demonstrated in the above cases, because the iBEM only uses mesh on the particle or inclusion and boundary elements, when particle moves in the matrix, the same mesh can be used.

Table 1
The effective modulus of the composite containing one 12.5% triangular inhomogeneity with different number of division seed, where soft and stiff represents the aluminum and steel inhomogeneities, respectively.

#*Seed*	#elements	$\overline{E}$ (soft) (GPa)	$\overline{\nu}$ (soft)	$\overline{E}$ (stiff) (GPa)	$\overline{\nu}$ (stiff)
1	1	173.699	0.304714	78.236	0.327353
2	4	173.704	0.304676	78.256	0.327304
3	9	173.706	0.304663	78.259	0.327299
5	25	173.708	0.304656	78.261	0.327294
15	181	173.708	0.304652	78.261	0.327294

4.4. Effective elasticity of a material sample

In Section 3, we have verified the iBEM algorithm with case studies of inclusion and inhomogeneity problems by comparisons with the FEM results for the local fields. Although the results for inhomogeneity problem are sensitive to the mesh, convergent results can be obtained with small number of elements. Even a single element provides a good prediction of the trend of the stress variation. For an actual material sample containing some inhomogeneities or particles, when we test the material properties, from the relationship of overall load and deformation, one can calculate the effective elasticity, which is based on the average stress and strain instead of the local elastic field. It creates a possibility that a very few elements in iBEM can predict the effective elastic moduli.

Actually, the iBEM is particularly suitable for the prediction of effective material properties by the boundary information. Given a test load on the boundary, say traction, the response of the displacement along the boundary can immediately provide information for the stiffness of the material system. Therefore, iBEM can be a powerful tool for virtual experiments. This section will illustrate the convergence of the effective elasticity with the number of elements in a particle and also the size of a representative volume of element (RVE).

In Fig. 9, with the refined global element size, the eigenstrain field exhibits mesh-related property merely in the neighborhood of the vertices, which implies the local field shares the same features. To investigate the effective mechanical behavior of the composites, several methods could be applied, such as (1) classic micromechanical analysis; (2) a unit cell under the periodic boundary conditions (PBC);(3) an adequately large RVE with a test loading. The limitation of micromechanical models have been discussed in the introduction, and the PBC will be implemented and discussed in this section. In the following, the effect of refinement of mesh on the effective modulus is investigated under the uni-axial loading.

4.4.1. Effective modulus for one triangular/tetrahedral inhomogeneity

In Fig. 2 of Section 3.1, one triangular/tetrahedral inhomogeneity is located inside a plate/cube (edge 20 cm). For the effective modulus test, the bottom constrained displacement condition is only applied to the x_2 direction, and the top pressure keeps the same as 1 MPa. Listed in Table 1, the effective modulus is collected with different size steps. Since the Eshelby's tensor is dimensionless, thus, instead of specifying the global element size, the number of division seed (#*Seed*) along the edge is applied.

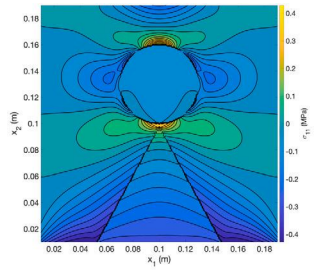

(a) σ_{11} of aluminum inhomogeneities

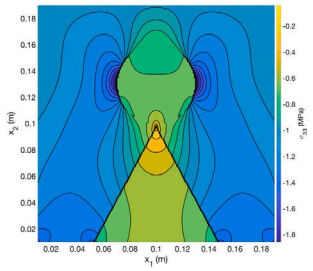

(b) σ_{22} of aluminum inhomogeneities

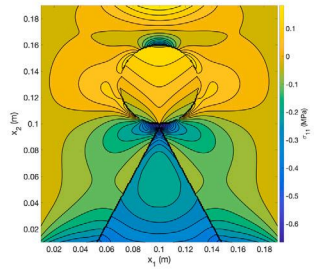

(c) σ_{11} of steel inhomogeneities

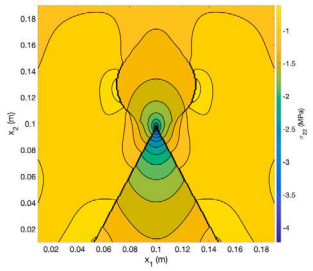

(d) σ_{22} of steel inhomogeneities

Fig. 16. Contour plot of the normal stresses field in the square of the range $x_1, x_2 \in [1, 19]$ cm for top-down circular and triangular inhomogeneity interactions under a uni-axial load.

Table 2
The effective modulus of the composite containing one 1.8% tetrahedral inhomogeneity with different number of division seed, where soft and stiff represents the aluminum and steel inhomogeneities, respectively.

#*Seed*	# elements	$\overline{E}$ (soft) (GPa)	$\overline{\nu}$ (soft)	$\overline{E}$ (stiff) (GPa)	$\overline{\nu}$ (stiff)
1	1	196.770	0.300111	71.397	0.329230
2	8	196.771	0.300098	71.411	0.329186
3	27	196.770	0.300094	71.413	0.329174
4	64	196.771	0.300092	71.414	0.329169
8	324	196.771	0.300092	71.414	0.329168

Table 3
The effective modulus of the composite containing one 30% triangular inhomogeneity with different number of division seed, where soft and stiff represents the aluminum and steel inhomogeneities, respectively.

#*Seed*	# elements	$\overline{E}$ (soft) (GPa)	$\overline{\nu}$ (soft)	$\overline{E}$ (stiff) (GPa)	$\overline{\nu}$ (stiff)
1	1	143.910	0.313749	91.949	0.324680
2	4	143.947	0.313584	91.999	0.324628
3	9	143.960	0.313544	92.003	0.324624
5	25	143.966	0.313522	92.008	0.324619
15	181	143.970	0.313511	92.009	0.324618
FEM	20,228	143.974	0.313353	92.004	0.324783

Table 4
The effective modulus of the composite containing one 6.6% tetrahedral inhomogeneity with different number of division seed, where soft and stiff represents the aluminum and steel inhomogeneities, respectively.

#*Seed*	# element	$\overline{E}$ (soft) (GPa)	$\overline{\nu}$ (soft)	$\overline{E}$ (stiff) (GPa)	$\overline{\nu}$ (stiff)
1	1	188.627	0.300792	75.328	0.327344
2	8	188.626	0.300730	75.388	0.327203
3	27	188.627	0.300718	75.400	0.327173
4	64	188.700	0.0.300704	75.441	0.327164
8	324	188.711	0.300696	75.450	0.327157

In Tables 1 and 2, we can observe the good convergence behavior of iBEM in the modeling of effective modulus. Let the bottom line data serve as the reference of convergent results, we can see the following aspects of the convergence of elastic moduli:

(1) For softer triangular inhomogeneity, $5.18 \times 10^{-3}\%, 2.30 \times 10^{-3}\%$, $1.15 \times 10^{-4}\%$ and 0;

(2) For stiffer triangular inhomogeneity, $3.19 \times 10^{-2}\%, 6.39 \times 10^{-3}\%$, $2.56 \times 10^{-3}\%$ and 0;

(3) For softer tetrahedral inhomogeneity, $5.08{\times}10^{-4}\%, 0, 5.08{\times}10^{-4}\%$ and 0;

(4) For stiffer tetrahedral inhomogeneity, $2.38 \times 10^{-2}\%, 4.2 \times 10^{-3}\%$, $1.4 \times 10^{-3}\%$ and 0.

Notice that the results are round to three decimal place, thus the difference 0 is actually a non-zero small number and can be neglected in the sense of engineering applications. In the above cases, a single element for one particle could provide an acceptable prediction of the effective, which saves efforts in computation and enables virtual experiments of large particle systems. However, the interactions between inhomogeneities and boundary is relatively low due to the low volume fraction. Hence, in the following case study, the volume fraction of triangle and tetrahedral inhomogeneity increase to 30% and 6.6% and the similar trends is exhibited in Tables 3 and 4, respectively. For a reference, an FEM case study is conducted with 20,228 elements for the 3D case with 30% of particles.

The differences between the 1 element (no discretization) case and the bottom line case do not exceed 0.14%, which implies that even the boundary interactions is considered, the iBEM still provide good results for very few element mesh. For the 2D case at 30%, comparing the FEM and 1 element iBEM case (due to symmetry of geometry and boundary conditions, only half domain is meshed for FEM.), the differences are:

(1) for soft inhomogeneity, $4.4{\times}10^{-2}\%$ and $1.26{\times}10^{-1}\%$ for young's modulus and Poisson's ratio, respectively;

(2) for stiff inhomogeneity, $5.97{\times}10^{-2}\%$ and $3.17{\times}10^{-2}\%$ for young's modulus and Poisson's ratio, respectively.

Considering its excellent convergence performance in prediction of effective modulus, even including the boundary and inhomogeneity interactions, only $\#Seed = 1, 2$ will be used in Section 4.4.2. The case studies of elliptical / ellipsoidal inhomogeneities can be referred in [1], and no repeat discussion will be added below. Here we show the case of multiple triangular/tetrahedral inhomogeneities.

Table 5
The effective modulus of the composite containing 25 triangular inhomogeneity (30% volume fraction) with different number of division seed, where soft and stiff represents the aluminum and steel inhomogeneities, respectively.

$\#Seed$	# elements	$\overline{E}$ (soft) (GPa)	$\overline{\nu}$ (soft)	$\overline{E}$ (stiff) (GPa)	$\overline{\nu}$ (stiff)
1	25	147.568	0.303659	94.958	0.317976
2	100	147.530	0.303955	94.980	0.317757

Table 6
The effective modulus of the composite containing 27 tetrahedral inhomogeneity (6.7% volume fraction) with different number of division seed, where soft and stiff represents the aluminum and steel inhomogeneities, respectively.

$\#Seed$	# elements	$\overline{E}$ (soft) (GPa)	$\overline{\nu}$ (soft)	$\overline{E}$ (stiff) (GPa)	$\overline{\nu}$ (stiff)
1	27	188.578	0.300192	75.437	0.326844
2	216	188.457	0.300196	75.571	0.326824

4.4.2. Effective modulus with multiple triangular/tetrahedral inhomogeneities

In this section, the particle interactions are introduced by adding more inhomogeneities into the simulation domain. Again, the effective moduli are compared through changing various division seed ($\#Seed$) of the edges. Without the loss of any generality, 25 equal sized isosceles and 64 tetrahedrons are uniformly distributed in the square/cube with the total volume fraction equals 30% and 6.6%, as illustrated in Section 5.1. Because Eshelby's tensor decreases rapidly with the distance between field and source point (Appendix D), thus it is reasonable to setup a global cutoff "distance ratio ρ" to minimize the computation efforts. Taking the 2D domain integral for instance, define $\rho = \frac{\mathcal{L}}{|\mathbf{x}'-\mathbf{x}|}$, where $\mathcal{L} = \sqrt{2A}$ is the characteristic length of the triangular element and A is the area. Similarly, define $\rho = (6V)^{1/3}$ for tetrahedral elements in 3D and V is the volume. When $\rho > 15$, the domain integral plays a small role in the elastic solution, hence, the contribution can be neglected. The cut-off can be redefined with the required accuracy. Notice that the choice of ρ may influence the accuracy of the solution, however, the accuracy could be compromised to save computational efforts if the error is controlled.

Shown in Tables 5 and 6 , when $\rho = 15$, the errors increase up to 0.82% but it is still acceptable with the single element case. Notice that if global cutoff is not considered, the effective young's modulus for are 147.544 GPa and 95.066 GPa for softer and stiffer inhomogeneity, respectively. Moreover, in the case of division seed $\#Seed$ at 2, the differences are comparatively small, which is due to the sizes of the element are larger, so the "cutoff" condition is not triggered frequently.

4.4.3. Effective modulus under periodic boundary condition

Directly applying a test load on the boundary of a small sample in the virtual experiments may not be representative for actual composites which cover a large area of volume. To consider the effective material properties of a composite, the periodic boundary condition (PBC) is commonly used on a unit cell to represent the microstructure features. The effective modulus can be calculated in the similar fashion from the averaged stress and strain relation under the PBC [1]. Fig. 17 illustrates the volume fraction of aluminum inhomogeneities varying from 0 to 40%. At each volume fraction step, 1, 9 and 25 equal-sized inhomogeneities are uniformly distributed in the square plate with the PBC.

Given a volume fraction of particles, the effective moduli can reach a convergent solution with one inhomogeneity unit cell under the PBC as it is overlapped with the cases of 9 or 25 particles, which is different from the virtual experiments in the last Section. Therefore, only one inhomogeneity could provide accurate results under the present case, because the interactions are partially considered in the PBC constraint equations in displacements and traction of the unit cell. However, it is observed that the disparity between the 9 case and 25 case starts when volume fraction is larger than 30%. Such phenomenons leave an initial

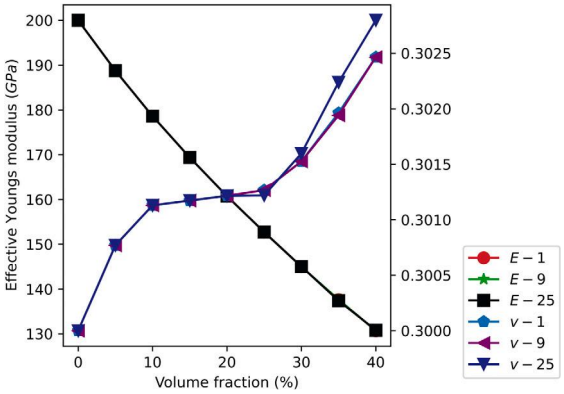

Fig. 17. Effective elastic moduli of inhomogeneities under the periodic boundary condition with 1,9 and 25 particles with the same boundary element mesh (400 elements).

impression that when the particle interactions become much more intensive, even the PBC cannot predict the effective moduli. However, it should still be cautious to generalize this observation to every case and particle interactions may be stronger for different shapes and stiffness ratios between the particle and matrix. In Fig. 17, the effective Young's modulus obtained under PBC are very close to each other with the inhomogeneity interactions; whereas the Poisson's ratio shows slight difference when the volume fraction is higher. Besides more intensive interactions, another issue is that the accuracy of boundary element part decreases due to the increase of inhomogeneities. Taking the 2D problem as example, in Section 3, 50 elements are applied for each edge of the square plate. Because the Eshelby's tensor is dimensionless, even the distance between particles and boundary decrease, the ratio between the distance and characteristic length of the particle remain the same, given the uniform alignment. Therefore, the interaction between particles and boundary does not change too much. However, when the particles are closer to the boundary, the accuracy decreases because fewer boundary elements are applied to describe the field. Shown in Fig. 17, the maximum error between case 25 and case 1 is 0.06%, which is small and the closer results (as 1) can be obtained through a refined boundary mesh (i.e., 1600 boundary elements).

For 3D problem, because the maximum volume fraction of a tetrahedron is $\frac{1}{6}$, to simulate higher volume fractions, a smaller cube is discretized with 12 tetrahedrons. Shown in Fig. 18, the effective moduli are compared with the classic micromechanical models, namely the dilute and Mori-Tanaka models [4] as reference. Notice that the two classic micromechanical models are based on the Eshelby's tensor of circular or spherical particles; whereas the present iBEM results are based on the angular particles, which is in between the two micromechanical models. Generally, the dilute model does not consider the interaction of inhomogeneities and underestimates the effective elasticity. Therefore, the iBEM results are reasonable. Although the local elastic field is significantly affected by the particle shape, the effective elasticity does not change significantly by the particle shape, but closely depends on the particle volume fraction. The iBEM provides a powerful tool to predict the effective stiffness of composites with arbitrarily shaped particles.

4.5. Virtual experiments of size gradation and random distribution of particles on the effective elasticity

In Section 4.4, the effective moduli are solved through uni-axial loading, unit cell under periodic boundary conditions and verified with FEM and micromechanical models. In this section, to exhibit the robustness of the method, instead of considering a RVE or unit cell, the virtual experiment with over 1,137 tetrahedral and 3,470 triangular

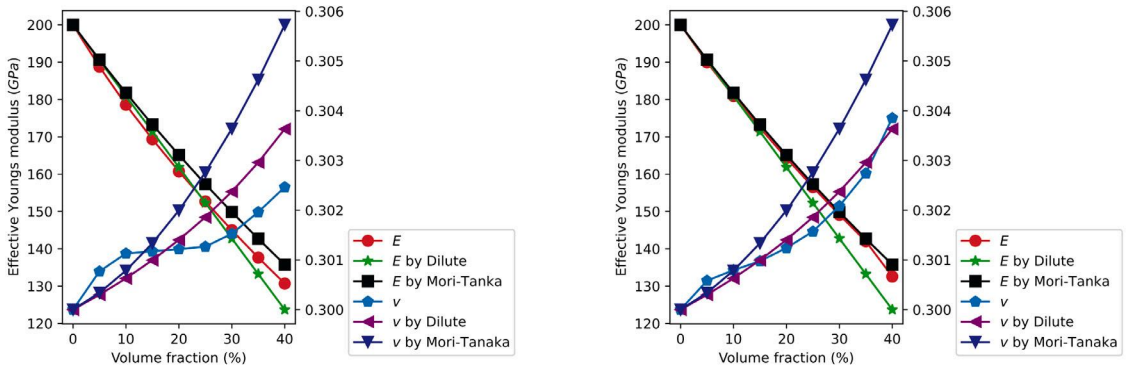

(a) 2D (b) 3D

Fig. 18. Comparison of the iBEM results with the dilute and Mori–Tanaka models for the effective elastic moduli of composites under the periodic boundary condition in (a) 2D and (b) 3D cases.

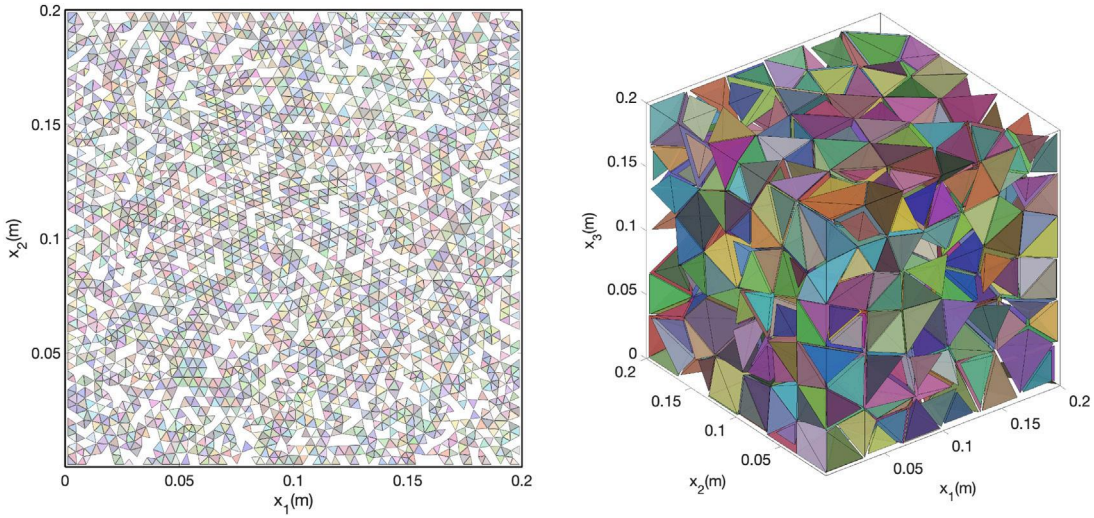

(a) 2D (b) 3D

Fig. 19. Schematic plot of 2D and 3D inhomogeneities distribution with 50% volume fraction.

particles are used for a composites with 50% volume fraction. Shown in Fig. 19, for example, 1591 triangular inhomogeneities are created in a 0.2 m × 0.2 m square plate. The mesh is generated by the following steps:

(1) Mesh the square with triangular elements;

(2) Use a pseudo-random function, which is written in combinations of "time.h" and "stdlib.h" to select the elements; (Notice that, the time library can generate random seeds, without which the randomness will not exist.) Since the elements are numbered in sequence, they can be selected with non-repeating generated random integers.

(3) In order to alter the size of elements, in step (2), setup a area/volume fraction (higher than the target), hence, some elements need to be shrunken accordingly. Use the pseudo-random function in (2) again, select elements and control the ratio of shrinking until the target is achieved. (Notice that if no requirement for the size difference, step (3) can be dropped by setting the target fraction in step (2).)

In Sections 4.4.1 and 4.4.2, we have demonstrated the good convergence performance with very few number of elements to represent an inhomogeneity. Therefore, in this section, triangles and tetrahedrons are represented by 1 element. Shown in Table 7, the effective moduli are compared with different numbers of inhomogeneities: for 2D problem, 6,500 and 3470 particles are included; whereas for 3D problem, 61,338 and 1137 particles are included, respectively. Although the orientation and size of particles are relatively random, the effective Young's modulus and Poisson's ratio are stable for the virtual experiments of the samples with different number of particles under the same volume fraction at 50%. The 3D case shows a lower Young's modulus than the 2D case.

Table 7
The effective modulus of virtual composite samples with 50% of aluminum particles randomly distributed in a steel matrix.

# 2D particles	$\overline{E}(GPa)(2D)$	$\overline{\nu}(2D)$	# 3D particles	$\overline{E}(GPa)(3D)$	$\overline{\nu}(3D)$
6	115.168	0.311444	61	125.776	0.305335
500	115.509	0.311746	338	124.4481	0.306705
3470	115.334	0.311482	1137	124.698	0.306706

5. Conclusions

This paper presents a novel numerical method, inclusion-based boundary element method (iBEM), to investigate the elastic fields for particulate composites containing arbitrarily shaped inhomogeneities. The material mismatch is simulated by an distributed eigenstrain on the particles. The displacement field is calculated by surface or line integral on the boundary and volume/area integral on the inclusions for 3D and 2D problems, respectively. For ellipsoidal or elliptical particles, the eigenstrain is written in the Taylor expansion at the centroid;

whereas for angular particles, domain discretization is used. The domain integral over the volume or area is conducted analytically with the exact solution, which leads to more rapid convergence with fewer elements. Adapted to various kinds of loading conditions, effective material properties are obtained through both virtual experiments or periodic boundary conditions. Some highlights of iBEM are provided as follows:

1. The iBEM predicts the stress singularity by Eshelby's tensor with high stability and convergence by particle discretization for polygonal particles;
2. The iBEM can provide very accurate prediction of local fields for composites containing arbitrarily shaped particles with analytical integrals of triangular and elliptical inclusions;
3. Because Eshelby's tensor is size independent, the iBEM can simulate a large size range of particles;
4. For angular particles, Eshelby's tensor handles with the singularity analytically. Although the eigenstrain exhibits singularity, its influence zone is very small and produce minor effects on overall accuracy;
5. No mesh is need in the matrix, so that iBEM can simulate the particle motion without the regeneration of mesh;
6. The iBEM can predict the effective material behaviors with a single or very few elements on each particle, so that virtual experiments of actual samples with a large number of particles can be conducted.

The virtual experiments with many particles show that the composite sample with randomly distributed particles can reach a convergent effective elasticity with relatively small number of particles. The method is general and its extension to multi-physical problems is underway.

Declaration of competing interest

The authors declare that they have no known competing financial interests or personal relationships that could have appeared to influence the work reported in this paper.

Acknowledgment

This work is sponsored by the National Science Foundation, United States IIP #1738802, IIP #1941244, CMMI#1762891, and U.S. Department of Agriculture NIFA #2021-67021-34201 whose support is gratefully acknowledged.

Appendix A. Inclusion problem with polynomial eigenstrains in a bounded domain

In Section 2.1, we introduced the boundary value problem of multiple subdomains, which can be assigned with various material properties. Notice that, the similar knowledge introduced in Appendix A can be found in our recent work [1], however, the appendix aims to introduce some background in Eshelby's problem. Before we consider the inhomogeneities in Fig. 1, following Eshelby's procedure [2], we can consider an inclusion problem that the subdomains exhibit the same stiffness as the matrix but is subjected to eigenstrains. Hereby, the eigenstrain is a generic term that refers to non-elastic strain, such as phase transformation, misfit or thermal strains. As illustrated in introduction and Fig. 8, the eigenstrain field for angular particles can barely be presented with a single polynomial terms. Thus, we propose a piece-wise continuous eigenstrain field on inclusions Ω^I only and zero on the matrix Ω^0, and this section the displacement field caused by such eigenstrain is given below.

$$\begin{aligned}&\int_D G_{ij}(\mathbf{x},\mathbf{x}')C^0_{mjkl}\varepsilon^*_{kl,m'}(\mathbf{x}')d\mathbf{x}'\\&=\int_{\partial D} G_{ij}(\mathbf{x},\mathbf{x}')C^0_{mjkl}\varepsilon^*_{kl}(\mathbf{x}')'n'_m d\mathbf{x}'-\int_D G_{ij,m'}(\mathbf{x},\mathbf{x}')C^0_{mjkl}\varepsilon^*_{kl}(\mathbf{x}')d\mathbf{x}'\\&=\int_D G_{ij,m}(\mathbf{x},\mathbf{x}')C^0_{mjkl}\varepsilon^*_{kl}(\mathbf{x}')d\mathbf{x}'\end{aligned}\tag{A.1}$$

where $\varepsilon^*_{kl}=0$ on ∂D and $G_{ij,m}=\frac{\partial G_{ij}}{\partial x_m}=-\frac{\partial G_{ij}}{\partial x'_m}=-G_{ij,m'}$ are used. Hence, Eq. (4) is derived. The third term in Eq. (4) is summation of influence brought by eigenstrain on every subdomain Ω^I and the boundary integrals can be evaluated by the original boundary element method in the next section. This section focuses on the domain integral for an inclusion Ω^I. Assume the eigenstrain is in the form of $\varepsilon^*_{ij}(\mathbf{x}')=\varepsilon^{*0}_{ij}+x'_k\varepsilon^{*1}_{ijk}+\mathcal{O}(x^2)$ on the inclusion, where the superscript 0 and 1 represents the uniform and linear orders of eigenstrain, respectively. For an elliptical/ellipsoidal subdomain, the integral of a polynomial eigenstrain up to the quadratic terms was derived [1]:

$$-\int_D G_{ij,m}(\mathbf{x},\mathbf{x}')C^0_{mjkl}\varepsilon^*_{kl}(\mathbf{x}')d\mathbf{x}'=g_{ikl}(\mathbf{x})\varepsilon^{*0I}_{kl}+g_{iklp}(\mathbf{x})\varepsilon^{*1I}_{klp}+g_{iklpq}(\mathbf{x})\varepsilon^{*2I}_{klpq}\tag{A.2}$$

where g_{ikl}, g_{iklp} and g_{iklpq} are the uniform, linear and quadratic Eshelby's tensor for displacements, which have been provided in details [1,4]. For polygonal/polyhedral subdomain, the $2D$ domain integral is provided in Section 2.2 and the $3D$ domain integral is enclosed in Appendix C. Rewrite Eq. (4) in terms of various domain integrals, i.e elliptical and polygons, the displacement and strain field (within D) can be expressed in Eq. (A.3) and (A.4), respectively,

$$\begin{aligned}u_i(\mathbf{x})=&-\sum_{e=1}^{N^b}H_{ij}u^e_j+\sum_{e=1}^{N^b}U_{ij}t^e_j+\left[\sum_{I=0}^{N^{ell}}g_{ikl}\varepsilon^{*0I}_{kl}+\sum_{I=0}^{N^{ell}}g_{iklp}\varepsilon^{*1I}_{klp}+\sum_{I=0}^{N^{ell}}g_{iklpq}\varepsilon^{*2I}_{klpq}\right]\\&+\frac{1}{8\pi(1-\nu)}\left[\sum_{J=0}^{N^p}(\mathcal{A}_{kl,kli}-2\nu\mathcal{B}_{kk,i}-4(1-\nu)\mathcal{B}_{lk,k})\right]\end{aligned}\tag{A.3}$$

$$\begin{aligned}\varepsilon_{im}(\mathbf{x})=&-\sum_{e=1}^{N^b}H_{imj}u^e_j+\sum_{e=1}^{N^b}U_{imj}t^e_j+\left[\sum_{I=0}^{N^{ell}}S_{imkl}\varepsilon^{*0I}_{kl}+\sum_{I=0}^{N^{ell}}S_{imklp}\varepsilon^{*1I}_{klp}\right.\\&\left.+\sum_{I=0}^{N^{ell}}S_{imklpq}\varepsilon^{*2I}_{klpq}\right]\\&+\frac{1}{8\pi(1-\nu)}\left\{\sum_{J=0}^{N^p}\left[\mathcal{A}_{kl,klim}-2\nu\mathcal{B}_{kk,im}-2(1-\nu)(\mathcal{B}_{ik,km}+\mathcal{B}_{mk,ki})\right]\right\}\end{aligned}\tag{A.4}$$

where S_{ijkl}, S_{ijklp} and S_{ijklpq} are Eshelby's tensor for uniform, linear and quadratic eigenstrain field, which can be derived by the compatibility law, i.e, $S_{ijkl}=\frac{1}{2}(g_{ikl,j}+g_{jkl,i})$; similarly, H_{imj} and U_{imj} denote the boundary integral of G_{ij} and T_{ij}, respectively. Hence, combining the boundary integral and domain integrals, the inclusion problem is solved.

Appendix B. Equivalent inclusion method for a bounded domain by the Taylor's expansion

In Appendix A, the inclusion problem is formulated as combination of boundary and domain integrals. Notice that, different to the inclusion problem with prescribed eigenstrain, eigenstrain (usually considered as misfit stain) is applied to simulate the material mismatch and required to be solved by the stress equivalent equation as follows,

$$C^0_{ijkl}:(\varepsilon^b_{kl}+\varepsilon'_{kl}-\varepsilon^*_{kl})=C^I_{ijkl}:(\varepsilon^b_{kl}+\varepsilon'_{kl})\tag{B.1}$$

where ε^b_{kl} and ε'_{kl} are the strains caused by the boundary and domain integral, respectively. It can be set up at many points in the particle as the algorithm for polygonal/polyhedral particles in Section 2.3 and Eq. (17). If the eigenstrain distribution is smooth, it can be represented by the eigenstrain at the centroid and its higher order derivatives in term of the Taylor's expansion on the point. Particularly, for elliptical/ellipsoidal particles, this method can be fast and accurate.

In [1,4,5], the elastic field can be solved in tailorable accuracy with polynomial-form eigenstrain and the equivalent conditions are listed below,

$$C^0_{ijkl} : (\varepsilon^b_{kl} + \varepsilon'_{kl} - \varepsilon^{*0I}_{kl}) = C^I_{ijkl} : (\varepsilon^b_{kl} + \varepsilon'_{kl}) \tag{B.2a}$$

$$C^0_{ijkl} : (\varepsilon^b_{kl,r} + \varepsilon'_{kl,r} - \varepsilon^{*1I}_{klr}) = C^I_{ijkl} : (\varepsilon^b_{kl,r} + \varepsilon'_{kl,r}) \tag{B.2b}$$

$$C^0_{ijkl} : (\varepsilon^b_{kl,rh} + \varepsilon'_{kl,rh} - \varepsilon^{*2I}_{klrh}) = C^I_{ijkl} : (\varepsilon^b_{kl,rh} + \varepsilon'_{kl,rh}) \tag{B.2c}$$

where ε^b_{kl} is the strain field by the boundary loading and ε'_{kl} is the disturbed strain field by eigenstrain, which could be derived from domain integrals of the Green's function and eigenstrain. The stress equivalent equations can be set up on the centroid of each particle for the constant, linear, and quadratic terms as follows:

$$\begin{aligned}
&\Delta C^I_{ijkl}\left(-\sum_{e=1}^{N^b} H_{klm}u^e_m + \sum_{e=1}^{N^b} U_{klm}t^e_m + \sum_{I=0}^{N^{ell}} S_{klab}\varepsilon^{*0I}_{ab} + \right.\\
&\left. + \sum_{I=0}^{N^{ell}} S_{klabp}\varepsilon^{*1I}_{abp} + \sum_{I=0}^{N^{ell}} S_{klabpq}\varepsilon^{*2I}_{abpq}\right)\\
&+ \frac{\Delta C^I_{ijkl}}{8\pi(1-\nu)}\left(\sum_{J=1}^{N^p}\left[\mathcal{A}_{kl,klij} - 2\nu\mathcal{B}_{kk,ij} - 2(1-\nu)(\mathcal{B}_{ik,kj} + \mathcal{B}_{jk,ki})\right]\right)\\
&+ C^0_{ijkl}\varepsilon^{*0I}_{kl} = 0
\end{aligned} \tag{B.3}$$

$$\begin{aligned}
&\Delta C^I_{ijkl}\left(-\sum_{e=1}^{N^b} H_{klrm}u^e_m + \sum_{e=1}^{N^b} U_{klrm}t^e_m + \sum_{I=0}^{N^{ell}} S_{klabr}\varepsilon^{*0I}_{ab}\right.\\
&\left. + \sum_{I=0}^{N^{ell}} S_{klabpr}\varepsilon^{*1I}_{abp} + \sum_{I=0}^{N^{ell}} S_{klabpqr}\varepsilon^{*2I}_{abpq}\right)\\
&+ \frac{\Delta C^I_{ijkl}}{8\pi(1-\nu)}\left(\sum_{J=1}^{N^p}\left[\mathcal{A}_{kl,klijr} - 2\nu\mathcal{B}_{kk,ijr} - 2(1-\nu)(\mathcal{B}_{ik,kjr} + \mathcal{B}_{jk,kir})\right]\right)\\
&+ C^0_{ijkl}\varepsilon^{*1I}_{klr} = 0
\end{aligned} \tag{B.4}$$

$$\begin{aligned}
&\Delta C^I_{ijkl}\left(-\sum_{e=1}^{N^b} H_{klrwm}u^e_m + \sum_{e=1}^{N^b} U_{klwrm}t^e_m + \sum_{I=0}^{N^{ell}} S_{klabrw}\varepsilon^{*0I}_{ab}\right.\\
&\left. + \sum_{I=0}^{N^{ell}} S_{klabprw}\varepsilon^{*1I}_{abp} + \sum_{I=0}^{N^{ell}} S_{klabpqrw}\varepsilon^{*2I}_{abpq}\right)\\
&+ \frac{\Delta C^I_{ijkl}}{8\pi(1-\nu)}\left(\sum_{J=1}^{N^p}\left[\mathcal{A}_{kl,klijrw} - 2\nu\mathcal{B}_{kk,ijrw} - 2(1-\nu)(\mathcal{B}_{ik,kjrw} + \mathcal{B}_{jk,kirw})\right]\right)\\
&+ C^0_{ijkl}(\varepsilon^{*2I}_{klrw} + \varepsilon^{*2I}_{klwr}) = 0
\end{aligned} \tag{B.5}$$

Notice that, this method has been used for triangle or tetrahedral elements as well [26,27], but the accuracy at the neighborhood of vertex is not good. Therefore, it is recommended to use this method on smooth particles and domain discretization on angular particles to get high accuracy. Assembly of the equations on the boundary nodes, Gaussian integral points for domain discretization, and centroids for elliptical/ellipsoidal inhomogeneities can establish the linear equation system. The numerical form is presented in Section 2.4.

Appendix C. Closed-form domain integral of 10-node quadratic tetrahedral element and closed-form of Φ_p

Consider the 10-node tetrahedral element, say (x^i_1, x^i_2, x^i_3), i = 1,2,3,4 are 4 corner nodes and i = 5, …, 10 are 6 mid-nodes for the 6 edges, the eigenstrain distribution in the element can be written in terms of eigenstrain on the nodes as,

$$\varepsilon^*_{ij}(\mathbf{x}') = \sum_{n=1}^{4}(2L^n - 1)L^n\,\varepsilon^{*n}_{ij} + \sum_{n=5}^{10} 4L^I L^J\,\varepsilon^{*n}_{ij} \tag{C.1}$$

where the superscript n represents the quantity associated with node n, and no index summation rule is applied with it; $\alpha^I, \beta^I, \gamma^I$ and χ^I are the components of the volume coordinates (linear shape function) of the Ith local corner node and the complete form can be written as $L^I = \alpha^I + \beta^I x^I_1 + \gamma^I x^I_2 + \chi^I x^I_3$ (let the other three local corner nodes be J, K, L, respectively).

$$\alpha^I = \frac{-x^L_1 x^K_2 x^J_3 + x^K_1 x^L_2 x^J_3 + x^L_1 x^J_2 x^K_3 - x^J_1 x^L_2 x^K_3 - x^K_1 x^J_2 x^L_3 + x^J_1 x^K_2 x^L_3}{6V} \tag{C.2a}$$

$$\beta^I = \frac{x^K_2 x^L_3 - x^L_2 x^J_3 - x^J_2 x^K_3 + x^L_2 x^K_3 + x^J_2 x^L_3 - x^K_2 x^L_3}{6V} \tag{C.2b}$$

$$\gamma^I = \frac{-x^K_1 x^J_3 + x^L_1 x^J_3 + x^J_1 x^K_3 - x^L_1 x^K_3 - x^J_1 x^L_3 + x^K_1 x^L_3}{6V} \tag{C.2c}$$

$$\chi^I = \frac{x^K_1 x^J_2 - x^L_1 x^J_2 - x^J_1 x^K_2 + x^L_1 x^K_2 + x^J_1 x^L_2 - x^K_1 x^L_2}{6V} \tag{C.2d}$$

where V is the volume of the element. For corner node I, the shape function is constructed as $(2L^I - 1)L^I$, whereas the one for mid-node between Ith and Jth corner nodes can be written as $4L^I L^J$. Obviously, the products of two shape functions contains uniform, linear and quadratic source terms, which can be treated in the same fashion as we derived the linear, quadratic potentials by separating the source terms into field and distance vector components [26,27]. Since the shape functions include the products of two corner nodes, in the following, we list the domain integral of L^I and $L^I L^J$ with $|\mathbf{x} - \mathbf{x}'|$ as an example to rearrange the terms of same order,

$$\Lambda^I = \int_{\omega^e} L^I |\mathbf{x} - \mathbf{x}'| d\mathbf{x}' = \alpha^I \Psi + \beta^I \Psi_1 + \gamma^I \Psi_2 + \chi^I \Psi_3 \tag{C.3a}$$

$$\begin{aligned}
\Lambda^{IJ} = \int_{\omega^e} L^I L^J |\mathbf{x} - \mathbf{x}'| d\mathbf{x}' &= \alpha^I\alpha^J\Psi + (\alpha^I\beta^J + \alpha^J\beta^I)\Psi_1\\
&+ (\alpha^I\gamma^J + \alpha^J\gamma^I)\Psi_2 + (\alpha^I\chi^J + \alpha^J\chi^I)\Psi_3\\
&+ (\beta^I\gamma^J + \beta^J\gamma^I)\Psi_{12} + (\beta^I\chi^J + \beta^J\chi^I)\Psi_{13} + (\beta^I\chi^J + \beta^J\chi^I)\Psi_{23}\\
&+ \beta^I\beta^J\Psi_{11} + \gamma^I\gamma^J\Psi_{22} + \chi^I\chi^J\Psi_{33}
\end{aligned} \tag{C.3b}$$

where Ψ_i and Ψ_{ij} are the linear and quadratic biharmonic potentials in [27]. Similarly, the domain integral of L^I and $L^I L^J$ with $|\mathbf{x} - \mathbf{x}'|^{-1}$ can be expressed by Γ^I and Γ^{IJ}, respectively.

The original form of Φ_p for 2D and 3D problem are listed below. Using Eq. (4) in [26] and Eq. (2) in [27] (direct area/volume integral), the Φ_p can be expressed for 2D and 3D problems, respectively, as follows:

$$\begin{aligned}
\Phi^{2D}_p = x_p\Phi + \sum_{I=1}^{N_I}\Big[&(\lambda^0_I)_p(\mathcal{H}_C(b_I, l^+_I) - \mathcal{H}_C(b_I, l^-_I))\\
&+ (\eta^0_I)_p(\mathcal{H}_S(b_I, l^+_I) - \mathcal{H}_S(b_I, l^-_I))\Big]
\end{aligned} \tag{C.4a}$$

$$\begin{aligned}
\Phi^{3D}_p = x_p\Phi + \sum_{I=1}^{N_I}\sum_{J=1}^{N_{JI}}\Big[\ &(\xi^0_I)_p(\mathcal{F}_H(a_I, b_{JI}, l^+_{JI}) - \mathcal{F}_H(a_I, b_{JI}, l^-_{JI}))\\
&+ (\lambda^0_{JI})_p(\mathcal{F}_C(a_I, b_{JI}, l^+_{JI}) - \mathcal{F}_C(a_I, b_{JI}, l^-_{JI}))\\
&+ (\eta^0_{JI})_p(\mathcal{F}_S(a_I, b_{JI}, l^+_{JI}) - \mathcal{F}_S(a_I, b_{JI}, l^-_{JI}))\Big]
\end{aligned} \tag{C.4b}$$

where λ^0_I and η^0_I are the unit outward normal and directional vector of the Ith edge of the polygons; ξ^0_I is unit outward normal vector of Ith surface of the polyhedron and; λ^0_{JI} and η^0_{JI} are the unit outward normal and directional vector of Jth edge of the Ith surface. Then, the analytical form of integrand functions are listed below,

$$\mathcal{H}_C(b, le) = \frac{b^2}{9}\left[8le - 6b\tan^{-1}[\frac{le}{b}] - 3le\ln[b^2 + le^2]\right] \tag{C.5a}$$

$$\mathcal{H}_S(b,le)=\frac{1}{18b}\left[5le^2-3le\ln[b^2+le^2]\right] \tag{C.5b}$$

$$\mathcal{F}_H(a,b,le)=\frac{a^2}{3b}\left[\,a|b|\sin^{-1}[\frac{ale}{\sqrt{(a^2+b^2)(b^2+le^2)}}]\right.$$
$$\left.+\,b\left(-|a|\tan^{-1}[\frac{le}{b}]+b\tanh^{-1}[\frac{le}{\sqrt{a^2+b^2+le^2}}]\right)\right] \tag{C.5c}$$

$$\mathcal{F}_C(a,b,le)=\frac{a}{6}\left[-\frac{a^2le}{\sqrt{b^2+le^2}}\tanh^{-1}[\frac{\sqrt{b^2+le^2}}{\sqrt{a^2+b^2+le^2}}]\right.$$
$$\left.+\,\frac{1}{2}(a^2+b^2)\ln[\frac{le+\sqrt{a^2+b^2+le^2}}{-le+\sqrt{a^2+b^2+le^2}}]\right] \tag{C.5d}$$

$$\mathcal{F}_S(a,b,le)=\frac{ab}{6}\left[\sqrt{a^2+b^2+le^2}+\frac{a^2}{\sqrt{b^2+le^2}}\tanh^{-1}[\frac{\sqrt{b^2+le^2}}{\sqrt{a^2+b^2+le^2}}]\right] \tag{C.5e}$$

Appendix D. Handling numerical singularities at interior nodes and the influence of the singularity at the vertices

The interior elastic field of stress and strain in inclusions or inhomogeneities should be continuous based on the continuum mechanics assumption. However, for triangular or tetrahedral domain integral, as the field point coincides with the interior node, there exists a mathematical singularity, which requires proper handling to evaluate the number. In the literature, this problem can be referred in [36,68] as the multi-region non-elastic problem, where some prescribed thermal/inelastic strain is given. The routine method is to isolate the singularity as follows:

(1) Generate a small circular (2D) / spherical (3D) exclusion zone, where the strain is caused by constant circular/spherical Eshelby's tensor multiplied with eigenstrain at the node;

(2) The singularities canceled out themselves at the infinitesimal circumference (2D) / shell (3D), thus the numerical integrals can be conducted. Our recent work [27] proposed a simpler alternative scheme, which abandons any numerical handling and it can be extended to 2D problem as well. Due to the assumption of distribution of eigenstrain by shape functions, the domain integral contains uniform, linear and quadratic terms of the eigenstrain distribution, in which the linear and quadratic Eshelby's tensors are written in terms of the uniform Eshelby's tensors and the distance vector [26,27] and the singularity is only generated by uniform Eshelby's tensors. When field point coincides with the interior nodes, all other shape functions at other nodes become 0, which implies the handling on the unit uniform tensors only. Using the divergence theorem, the unit uniform tensor is transferred to contour integrals, where no singularity exists any more and the number can be evaluated exactly by avoiding the numerical singularity in the mathematical formulation.

For a field point at a vertex, the singularity of Eshelby's tensor will create the stress singularity in the inclusion problem. Because of the $\ln r$ singularity of the Eshelby's tensor at a vertex of a triangular inhomogeneity in 2D problems, the eigenstrain also exhibits a $\ln r$ singularity or approaches zero at the vertex. For the 3D problem, the $\ln r$ singularity of Eshelby's tensor will exhibit on the edge of an angular particle similarly to the 2D problem; whereas the $\frac{1}{r}$ singularity can be found at the vertex [20,27]. We can show the stress singularity for the inhomogeneity problem as below.

Without loss of generality, we investigate the singularity at the top vertex of a tetrahedral inhomogeneity embedded in an infinite domain D subjected to a far field stress σ^0_{ij} as Fig. D.20 in the Cartesian Coordinate with the origin at the top vertex, in which an eigenstrain on the particle is introduced to simulate the stiffness mismatch between the inhomogeneity and matrix. If the stress equivalent condition in Eq. (6) is satisfied at each position on the inhomogeneity, the equivalent inclusion problem provides the exact solution to the inhomogeneity problem. Due to the singularity of Eshelby's tensor [20], the distribution of eigenstrain in the neighborhood of the vertex is open for investigation.

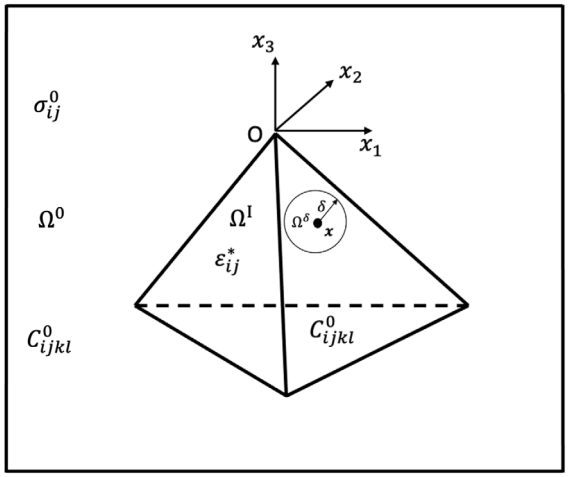

Fig. D.20. An equivalent tetrahedral inhomogeneity Ω^I with ε^0_{ij} embedded in the infinite domain Ω^0 subjected to a prescribed stress σ^0_{ij}.

Because ε'_{kl} is singular at the vertex for the inclusion problem, the stress equivalent equation cannot be established exactly at the vertex, which may produce a misconception that the eigenstrain must approach the infinite at the vertex as well. Following we can investigate the distribution of mismatch eigenstrain in the particle.

In Fig. D.20, a tiny spherical area Ω^δ with the radius of δ and the center at $\mathbf{x}^0$ is introduced. The integral of ε'_{kl} over Ω^δ can be written as

$$\begin{aligned}\int_{\Omega^\delta}\varepsilon'_{kl}(\mathbf{x})d\mathbf{x}&=-\frac{1}{2}\int_{\Omega^\delta}\int_{\Omega}[G_{ki,jl}(\mathbf{x},\mathbf{x}')+G_{li,jk}(\mathbf{x},\mathbf{x}')]C^0_{ijmn}\varepsilon^*_{mn}(\mathbf{x}')d\mathbf{x}'d\mathbf{x}\\&=\int_{\Omega}\int_{\Omega^\delta}\overline{G}_{klmn}(\mathbf{x},\mathbf{x}')d\mathbf{x}\varepsilon^*_{mn}(\mathbf{x}')d\mathbf{x}'\\&=\int_{\Omega}S^\delta_{klmn}(\mathbf{x}'-\mathbf{x}^0)\varepsilon^*_{mn}(\mathbf{x}')d\mathbf{x}'\end{aligned} \tag{D.1}$$

where

$$\begin{aligned}\overline{G}_{klmn}(\mathbf{x},\mathbf{x}')&=-\frac{1}{2}[G_{ki,jl}(\mathbf{x},\mathbf{x}')+G_{li,jk}(\mathbf{x},\mathbf{x}')]C^0_{ijmn}\\&=\frac{1}{8\pi(1-\nu)|\mathbf{x}-\mathbf{x}'|^3}[-(1-2\nu)\delta_{kl}\delta_{mn}\\&+(1-2\nu)(\delta_{km}\delta_{ln}+\delta_{kn}\delta_{lm})\\&+3\delta_{kl}n_mn_n+3(1-2\nu)\delta_{mn}n_kn_l\\&+3\nu(\delta_{km}n_nn_l+\delta_{lm}n_nn_k+\delta_{kn}n_mn_l+\delta_{ln}n_mn_k)-15n_kn_ln_mn_n]\end{aligned} \tag{D.2}$$

in which $\mathbf{n}=\frac{\mathbf{x}'-\mathbf{x}}{|\mathbf{x}'-\mathbf{x}|}$ and $S^\delta_{klmn}(\mathbf{x}'-\mathbf{x}^0)$ is the Eshelby's tensor for the small domain Ω^δ.

$$S^\delta_{klmn}(\mathbf{x}'-\mathbf{x}^0)=\begin{cases}\frac{5\nu-1}{15(1-\nu)}\delta_{kl}\delta_{mn}+\frac{4-5\nu}{15(1-\nu)}(\delta_{km}\delta_{ln}+\delta_{kn}\delta_{lm}), & \underline{\textbf{for}\,\mathbf{x}'\in(\Omega^\delta)}\\ \frac{\rho^3}{30(1-\nu)}[(3\rho^2+10\nu-5)\delta_{kl}\delta_{mn}\\ +(3\rho^2-10\nu+5)(\delta_{km}\delta_{ln}+\delta_{kn}\delta_{lm})\\ +15(1-\rho^2)\delta_{kl}n_mn_n+15(1-2\nu-\rho^2)\delta_{mn}n_kn_l\\ +15(\nu-\rho^2)(\delta_{km}n_nn_l+\delta_{lm}n_nn_k+\delta_{kn}n_mn_l+\delta_{ln}n_mn_k)\\ +15(7\rho^2-5)n_kn_ln_mn_n], & \underline{\textbf{for}\,\mathbf{x}'\notin(\Omega^\delta)}\end{cases} \tag{D.3}$$

where $\rho = \frac{\delta}{|\mathbf{x}'-\mathbf{x}^0|}$ and $n_i = \frac{x_i'-x_i^0}{|\mathbf{x}'-\mathbf{x}^0|}$ with $\mathbf{x}$ replaced by the sphere center at $\mathbf{x}^0$ in Eq. (D.2). For $\mathbf{x}' \in \Omega^\delta$, Eshelby's tensor is a constant, namely S^c_{klmn}. For $\mathbf{x}' \notin \Omega^\delta$ or $|\mathbf{x}'-\mathbf{x}^0| > \delta$, comparing Eqs. (D.2) and (D.3), one can rewrite the Eshelby's tensor as follows:

$$\begin{aligned} S^\delta_{klmn}(\mathbf{x}'-\mathbf{x}^0) = {} & \frac{4\pi\delta^3}{3}\overline{G}_{klmn}(\mathbf{x}',\mathbf{x}^0) + \frac{\delta^5}{10(1-\nu)(|\mathbf{x}'-\mathbf{x}^0|)^5} \\ & [\delta_{kl}\delta_{mn} + \delta_{km}\delta_{ln} + \delta_{kn}\delta_{lm} \\ & - 5\left(\delta_{kl}n_mn_n + \delta_{mn}n_kn_l + \delta_{km}n_nn_l + \delta_{lm}n_nn_k + \delta_{kn}n_mn_l + \delta_{ln}n_mn_k\right) \\ & + 35n_kn_ln_mn_n] \end{aligned} \tag{D.4}$$

Here Eshelby's tensor can evaluate the strain caused by a unit uniform eigenstrain over a source domain, which is applicable to an arbitrary shape. It exhibits the following properties:

(1) Eshelby's tensor $\mathbf{S}$ is dimensionless and its distribution depends on the shape of source domain and relative location. The integral of Eshelby's tensor of an inclusion over the inclusion itself is proportional to the area or volume, referred to the similar shape of inclusion with a unit area or volume for 2D and 3D cases respectively.

(2) Although Eshelby's tensor $\mathbf{S}$ may exhibit a $\frac{1}{r}$ singularity at the neighborhood of an vertex, its integral over the inclusion is positive definite and bounded with $\mathbf{0} < \int_\Omega \mathbf{S}(\mathbf{x}')d\mathbf{x}' < V\mathbf{I}$, where V is the volume of the inclusion and the unit tensor $I_{klmn} = \frac{1}{2}\left(\delta_{km}\delta_{ln} + \delta_{kn}\delta_{lm}\right)$.

(3) The Eshelby's tensor of an area formed by the complement of a large inclusion including a small one is the difference of the Eshelby's tensor of the larger triangle from the smaller one.

Now consider the eigenstrain distribution in the tetrahedron in Fig. D.20. First let $\Omega^\delta \in \Omega$, so that its center $\mathbf{x}^0$ cannot be either on the boundary or outside of Ω. The integral of Eq. (D.1) can be written in two parts from Ω^δ and $\overline{\Omega}$ with their areas indicated by V^δ and $\overline{V}$. Because Eq. (B.1) is supposed to be satisfied at every point on the triangle Ω, with the aid of Eq. (D.1), the integral of Eq. (B.1) over Ω^δ can be written as

$$\begin{aligned} \Delta C_{ijkl}\Bigg[& V^\delta\varepsilon^0_{kl} + \int_{\Omega^\delta} S^\delta_{klmn}(\mathbf{x}'-\mathbf{x}^0)\varepsilon^*_{mn}(\mathbf{x}')d\mathbf{x}' \\ & + \int_{\overline{\Omega}} S^\delta_{klmn}(\mathbf{x}'-\mathbf{x}^0)\varepsilon^*_{mn}(\mathbf{x}')d\mathbf{x}'\Bigg] + V^\delta C^0_{ijkl} : \varepsilon^{*\delta}_{kl} = 0 \end{aligned} \tag{D.5}$$

where $V^\delta = \frac{4\pi\delta^3}{3}$ is the volume of Ω^δ, $\Delta C_{ijkl} = C^1_{ijkl} - C^0_{ijkl}$ and ${\varepsilon_{mn}}^{*\delta}$ is the average eigenstrain of sphere ω^δ. The Eshelby's tensor in the second term of the above equation is a constant, namely S^c_{klmn}, as the eigenstrain is within the sphere. The third term is well defined because $|\mathbf{x}'-\mathbf{x}^0| > \delta$ in the domain $\overline{\Omega}$. Due to the continuity of eigenstrain, Using the mean value theorem (MVT), Eq. (D.5) can be rewritten as follows:

$${\varepsilon_{ij}}^{*\delta} = -\left(S^c_{ijkl} + \Delta C^{-1}_{ijpq}C^0_{pqkl}\right)^{-1}\left[\varepsilon^0_{kl} + \frac{1}{V^\delta}\int_{\overline{\Omega}} S^\delta_{klmn}(\mathbf{x}'-\mathbf{x}^0)d\mathbf{x}'\overline{\varepsilon}^*_{mn}\right] \tag{D.6}$$

where $\overline{\varepsilon}^*_{mn}$ is the eigenstrain a certain point in $\overline{\Omega}$. Using Eq. (D.4), when $\delta \to 0$, the higher order term of δ^5 will decay to zero rapidly, and the last term in the above equation can be rewritten

$$\frac{1}{V^\delta}\int_{\overline{\Omega}} S^\delta_{klmn}(\mathbf{x}'-\mathbf{x}^0)d\mathbf{x}' = \int_{\overline{\Omega}} \overline{G}_{klmn}(\mathbf{x}',\mathbf{x}^0)d\mathbf{x}' = S^\Omega_{klmn}(\mathbf{x}^0) - S^c_{klmn} \tag{D.7}$$

where $S^\Omega_{klmn}(\mathbf{x}^0)$ is the Eshelby's tensor of the large tetrahedron Ω at $\mathbf{x}^0$. Here Property 3 is used. For $\delta \to 0$, Eq. (D.6) defines the eigenstrain at $\mathbf{x}^0$ as

$${\varepsilon_{ij}}^{*\delta} = -\left(S^c_{ijkl} + \Delta C^{-1}_{ijpq}C^0_{pqkl}\right)^{-1}\left[\varepsilon^0_{kl} + \left(S^\Omega_{klmn}(\mathbf{x}^0) - S^c_{klmn}\right)\overline{\varepsilon}^*_{mn}\right] \tag{D.8}$$

If $\mathbf{x}^0$ is far from the vertices, $S^\Omega_{klmn}(\mathbf{x}^0)$ is well defined and bounded. Based on Property 2, $S^c_{ijkl} + \Delta C^{-1}_{ijpq}C^0_{pqkl} \neq \mathbf{0}$. Therefore, the above equation can be solved. When $\mathbf{x}^0 \to \mathbf{0}$, $S^\Omega_{klmn}(\mathbf{x}^0) \propto \frac{1}{|\mathbf{x}^0|}$. Therefore, ${\varepsilon_{ij}}^{*\delta}$ may exhibit a singularity of $\frac{1}{r}$ when $\overline{\varepsilon}^*_{mn}$ is non-zero.

Notice that $\overline{\varepsilon}^*_{mn}$ is located within $\overline{\Omega}$, but it can change with $\mathbf{x}^0$ and approach zero. Therefore it can be related to ${\varepsilon_{ij}}^{*\delta}$ as

$${\varepsilon_{ij}}^{*\delta} = R_{ijmn}\overline{\varepsilon}^*_{mn} \tag{D.9}$$

where R_{ijmn} defines their relationship. Therefore, Eq. (D.8) can be rewritten as

$$\varepsilon^{*\delta}_{ij} = -\left[S^c_{ijkl} + \Delta C^{-1}_{ijpq}C^0_{pqkl} + (S^\Omega_{ijmn}(\mathbf{x}^0) - S^c_{ijmn})R^{-1}_{mnkl}\right]^{-1}\varepsilon^0_{kl} \tag{D.10}$$

If $\mathbf{R}$ is a definite tensor between $\mathbf{0}$ and ∞, Eq. (D.10) will provide $\varepsilon^{*\delta}_{ij} \to \mathbf{0}$ because $S^\Omega_{ijmn}(\mathbf{x}^0) \to \infty$, which makes $\mathbf{R} \to 0$. Therefore, $\mathbf{R}$ can only be either $\mathbf{0}$ or ∞. Moreover, when $\mathbf{R} \to 0$, to make a definite eigenstrain at the neighborhood of the vertex, it must exhibit a convergent rate of r. Therefore, we can make the following conclusion:

When an angular elastic inhomogeneity embedded in another 3D elastic solid is subject to an external load, the mismatch eigenstrain approaches either zero or the infinite at a rate of r or $\frac{1}{r}$, respectively, which leads to the stress singularity up to $\frac{1}{r^2}$.

Now consider a continuously distributed eigenstrain field with the eigenstrain singularity of $\frac{1}{r}$ in the neighborhood of the vertex in Fig. D.20. Although the stress at the vertex will exhibit a $\frac{1}{r^2}$ singularity at the vertex because the eigenstrain approach the infinite at a rate of $\frac{1}{r}$. Its influence to a field point $\mathbf{x}$ far from the vertex is provided as follows. From Eqs. (8) and (D.2), the influence decays at $\frac{1}{r^3}$, and the contribution of the singular eigenstrain in Ω^δ to the strain at a point $\mathbf{x}$ far from Ω^δ can be written as

$$\varepsilon'_{kl}(\mathbf{x}) = \int_{\Omega^\delta} \overline{G}_{klmn}(\mathbf{x},\mathbf{x}')\varepsilon^*_{mn}(\mathbf{x}')d\mathbf{x}' = \overline{G}_{klmn}(\mathbf{x},\mathbf{x}^a)\int_{\Omega^\delta}\varepsilon^*_{mn}(\mathbf{x}')d\mathbf{x}' \tag{D.11}$$

where $\mathbf{x}^a \in \Omega^\delta$. Here the MVT is used because $\overline{G}_{klmn}(\mathbf{x},\mathbf{x}')$ is well defined for $\mathbf{x}$ is out of Ω^δ and $\varepsilon^*_{mn}(\mathbf{x}')d\mathbf{x}' = \varepsilon^*_{mn}(\mathbf{x}')r^2drd\Sigma$ with $d\Sigma$ being the unit sphere surface is well defined too [4]. In other words, a singularity of the eigenstrain at the rate of $\frac{1}{r}$ in the expression of $\frac{1}{r}d\mathbf{x}'$ is transferred to $rdrd\Sigma$, which is without singularity, so that the MVT is applicable. When $\delta \to 0$, one can obtain $\mathbf{x}^a \to \mathbf{0}$, so that the contribution of the singular eigenstrain at the vertex decays at the rate of $\frac{1}{r^3}$ based on the definition of $\overline{G}_{klmn}$ in Eq. (D.2). Therefore, although the value of eigenstrain on the vertex is not defined, its effect to the overall solution is minimal. That is the reason why a single element for one particle can provide fairly acceptable results with the iBEM.

Appendix E. Handling of the strong singularities in conventional BEM global matrix

In Eq. (18), the iBEM algorithm is illustrated explicitly in the matrix form, which is composed of the conventional BEM part (dealing with the boundary conditions) and the inclusion part (dealing with the particle material mismatch). The singularity issue for inclusion part is handled by a subdomain collocation method as discussed in Sections 2.2 and 2.3. Regarding the conventional BEM part, when the source point coincides with the field point, there exists strong singularity for the fundamental solution of traction, which leads to numerical difficulty to calculate the diagonal element of the H matrix containing Cauchy principal value integrals. Instead of direct mathematical integral, Beer et al. [36] proposed an indirect method using the rigid-body motion scheme to calculate the diagonal element of H, say H_{II}. Consider a unit displacement field for all nodes (like a rigid-body motion) without any traction on the boundary, which should be an allowable solution and satisfy the same linear equation system. Because the displacement and traction are given as 1 and 0, respectively, we can use the linear equation system to calculate the diagonal element of H instead. Therefore, the Cauchy principal value integrals are avoided and the diagonal components of H matrix are calculated as the summation of other elements in the same row as,

$$H_{II} = \sum_{J=1,J\neq I}^{N} H_{IJ} \tag{E.1}$$

where N is the total dimension number in the global matrix related to the displacements of boundary nodes.

In order to better describe the scheme in the matrix form for programming purposes, we form two matrices instead: H_{IJ} with all diagonal elements being zero, $Q_{II} = H_{II}$ as a diagonal matrix. The sum of $H + Q$ is what we need to set up the linear equations system.

References

[1] Wu Chunlin, Yin Huiming. The inclusion-based boundary element method (iBEM) for virtual experiments of elastic composites. Eng Anal Bound Elem 2021;124:245–58.

[2] Eshelby John Douglas. The determination of the elastic field of an ellipsoidal inclusion, and related problems. Proc R Soc Lond A 1957;241(1226):376–96.

[3] Sendeckyj GP. Ellipsoidal inhomogeneity problem (Ph.D. thesis), Northwestern University, Evanston; 1967.

[4] Mura Toshio. Micromechanics of defects in solids. Springer Netherlands; 1987.

[5] Moschovidis ZA, Mura T. Two-ellipsoidal inhomogeneities by the equivalent inclusion method. J Appl Mech 1975;42(4):847–52.

[6] Shodja HM, Rad IZ, Soheilifard R. Interacting cracks and ellipsoidal inhomogeneities by the equivalent inclusion method. J Mech Phys Solids 2003;51(5):945–60.

[7] Jin Xiaoqing, Keer Leon M, Wang Qian. A closed-form solution for the Eshelby tensor and the elastic field outside an elliptic cylindrical inclusion. J Appl Mech 2011;78(3).

[8] Ma HM, Gao X-L. Eshelby's tensors for plane strain and cylindrical inclusions based on a simplified strain gradient elasticity theory. Acta Mech 2009;211(1–2):115–29.

[9] Gao X-L, Ma HM. Strain gradient solution for Eshelby's ellipsoidal inclusion problem. Proc R Soc A 2010;466(2120):2425–46.

[10] Dang Xiangxin, Liu Yingjie, Wang Linjuan, Wang Jianxiang. Solutions of the elastic fields in a half-plane region containing multiple inhomogeneities with the equivalent inclusion method and the applications to properties of composites. Acta Mech 2019;230(5):1529–47.

[11] Song G, Wang L, Deng L, Yin HM. Mechanical characterization and inclusion based boundary element modeling of lightweight concrete containing foam particles. Mech Mater 2015;91:208–25.

[12] Liu YJ, Song G, Yin HM. Boundary effect on the elastic field of a semi-infinite solid containing inhomogeneities. Proc R Soc A 2015;471(2179):20150174.

[13] Liu MQ, Gao X-L. Strain gradient solution for the Eshelby-type polygonal inclusion problem. Int J Solids Struct 2013;50(2):328–38.

[14] Chiu YP. On the stress field due to initial strains in a cuboid surrounded by an infinite elastic space. J Appl Mech 1977;44(4):587–90.

[15] Chiu YP. On the stress field and surface deformation in a half space with a cuboidal zone in which initial strains are uniform. J Appl Mech 1978;45(2):302–6.

[16] Chiu YP. On the internal stresses in a half plane and a layer containing localized inelastic strains or inclusions. J Appl Mech 1980;47(2):313–8.

[17] Mura T. The determination of the elastic field of a polygonal star shaped inclusion. Mech Res Commun 1997;24(5):473–82.

[18] Furuhashi R, Mura T. On the equivalent inclusion method and impotent eigenstrains. J Elasticity 1979;9(3):263–70.

[19] Ru CQ. Analytic solution for Eshelby's problem of an inclusion of arbitrary shape in a plane or half-plane. J Appl Mech 1999;66(2):315–523.

[20] Rodin Gregory J. Eshelby's inclusion problem for polygons and polyhedra. J Mech Phys Solids 1996;44(12):1977–95.

[21] Nozaki H, Taya M. Elastic fields in a polygon-shaped inclusion with uniform eigenstrains. J Appl Mech 1997;64(3):495–502.

[22] Nozaki H, Taya M. Elastic fields in a polyhedral inclusion with uniform eigenstrains and related problems. J Appl Mech 2000;68(3):441–52.

[23] Trotta S, Marmo F, Rosati L. Evaluation of the Eshelby tensor for polygonal inclusions. Composites B 2017;115:170–81.

[24] Zou Wennan, He Qichang, Huang Mojia, Zheng Quanshui. Eshelby's problem of non-elliptical inclusions. J Mech Phys Solids 2010;58(3):346–72.

[25] Li Pu, Zhang Xiangning, An Yuhuan, Zhang Rui, Jin Xiaoqing, Hu Ning, Keer Leon M. Analytical solution for the displacement of a polygonal inclusion with a special application to the case of linear eigenstrain. Eur J Mech A Solids 2020;84:104049.

[26] Wu Chunlin, Yin Huiming. Elastic solution of a polygon-shaped inclusion with a polynomial eigenstrain. J Appl Mech 2021;1–25.

[27] Wu Chunlin, Zhang Liangliang, Yin Huiming. Elastic solution of a polyhedral particle with a polynomial eigenstrain and particle discretization. J Appl Mech 2021;1–35.

[28] Sevostianov Igor, Kachanov Mark. Relations between compliances of inhomogeneities having the same shape but different elastic constants. Internat J Engrg Sci 2007;45(10):797–806.

[29] Wen-Nan Zou Quan-Shui Zheng. The second Eshelby problem and its solvability. Acta Mech Sinica 2012;28(5):1331.

[30] Nakasone Yuji, Nishiyama Hirotada, Nojiri Tetsuharu. Numerical equivalent inclusion method: a new computational method for analyzing stress fields in and around inclusions of various shapes. Mater Sci Eng A 2000;285(1–2):229–38.

[31] Zhou Qinghua, Jin Xiaoqing, Wang Zhanjiang, Wang Jiaxu, Keer Leon M, Wang Qian. Numerical implementation of the equivalent inclusion method for 2D arbitrarily shaped inhomogeneities. J Elasticity 2014;118(1):39–61.

[32] Jiahui Hou, Pu Li, Jianglin Li, Xiaoqing Jin. A triangular element discretization for computing dispalcement of an arbitrarily shaped thermal inclusion. Chin J Theor Appl Mech 2021.

[33] Huiming Yin Yingtao Zhao. Introduction to the micromechanics of composite materials. CRC PR INC; 2016.

[34] Kanit T, Forest S, Galliet I, Mounoury V, Jeulin D. Determination of the size of the representative volume element for random composites: statistical and numerical approach. Int J Solids Struct 2003;40(13–14):3647–79.

[35] Yin HM, Buttlar WG, Paulino GH, Benedetto H Di. Assessment of existing micromechanical models for asphalt mastics considering viscoelastic effects. Road Mater Pavement Design 2008;9(1):31–57.

[36] Gernot Beer Ian M Smith, Duenser Christian. The boundary element method with programming. Springer Vienna; 2008.

[37] Hiroshi Hatta, Minoru Taya. Equivalent inclusion method for steady state heat conduction in composites. Internat J Engrg Sci 1986;24(7):1159–72.

[38] Huang Quan-Zhang, Xu Zhi-Gao, Qiang Hong-Fu, Wang Guang, Zheng Xiao-Ping. Boundary element method for solid materials with multiple types of inclusions. Acta Mech 2014;226(2):547–70.

[39] Beer Gernot, Dünser Christian, Ruocco Eugenio, Mallardo Vincenzo. Efficient simulation of inclusions and reinforcement bars with the isogeometric boundary element method. Comput Methods Appl Mech Engrg 2020;372:113409.

[40] Helsing Johan. Fast and accurate numerical solution to an elastostatic problem involving ten thousand randomly oriented cracks. Int J Fract 2000;100(4):321–7.

[41] Fu Yuhong, Klimkowski Kenneth J, Rodin Gregory J, Berger Emery, Browne James C, Singer Jürgen K, Geijn Robert AVan De, Vemaganti Kumar S. A fast solution method for three-dimensional many-particle problems of linear elasticity. Internat J Numer Methods Engrg 1998;42(7):1215–29.

[42] Fu Yuhong, Rodin Gregory J. Fast solution method for three-dimensional Stokesian many-particle problems. Commun Numer Methods Eng 2000;16(2):145–9.

[43] Lai Yi-Shao, Rodin Gregory J. Fast boundary element method for three-dimensional solids containing many cracks. Eng Anal Bound Elem 2003;27(8):845–52.

[44] Liu YJ. A fast multipole boundary element method for 2D multi-domain elastostatic problems based on a dual BIE formulation. Comput Mech 2008;42(5):761–73.

[45] Liu YJ, Shen L. A dual BIE approach for large-scale modelling of 3-D electrostatic problems with the fast multipole boundary element method. Internat J Numer Methods Engrg 2007;71(7):837–55.

[46] Wu Zhipeng, Lin Qinye, Chen Yongqiang. Application of fast multipole boundary element method for two-dimensional nonlinear interface debonding of particulate composites. Eng Anal Bound Elem 2020;113:72–81.

[47] Dong CY, Lo SH, Cheung YK. Application of the boundary-domain integral equation in elastic inclusion problems. Eng Anal Bound Elem 2002;26(6):471–7.

[48] Ma Hang, Guo Zhao, Dhanasekar Manicka, Yan Cheng, Liu Yijun. Efficient solution of multiple cracks in great number using eigen COD boundary integral equations with iteration procedure. Eng Anal Bound Elem 2013;37(3):487–500.

[49] Ma Hang, Yan Cheng, hua Qin Qing. Eigenstrain boundary integral equations with local Eshelby matrix for stress analysis of ellipsoidal particles. Math Probl Eng 2014;2014:1–10.

[50] Nardini D, Brebbia CA. A new approach to free vibration analysis using boundary elements. Appl Math Model 1983;7(3):157–62.

[51] Agnantiaris JP, Polyzos D, Beskos DE. Some studies on dual reciprocity BEM for elastodynamic analysis. Comput Mech 1996;17(4):270–7.

[52] Zhou Fenglin, Zhang Jianming, Sheng Xiaomin, Li Guangyao. A dual reciprocity boundary face method for 3D non-homogeneous elasticity problems. Eng Anal Bound Elem 2012;36(9):1301–10.

[53] Hsiao S-C, Mammoli AA, Ingber MS. The evaluation of domain integrals in complex multiply-connected three-dimensional geometries for boundary element methods. Comput Mech 2003;32(4–6):226–33.

[54] Ingber Marc S, Mammoli Andrea A, Brown Mary J. A comparison of domain integral evaluation techniques for boundary element methods. Internat J Numer Methods Engrg 2001;52(4):417–32.

[55] Hughes TJR, Cottrell JA, Bazilevs Y. Isogeometric analysis: CAD, finite elements, NURBS, exact geometry and mesh refinement. Comput Methods Appl Mech Engrg 2005;194(39–41):4135–95.

[56] Ghorashi Seyed Shahram, Valizadeh Navid, Mohammadi Soheil. Extended isogeometric analysis for simulation of stationary and propagating cracks. Internat J Numer Methods Engrg 2011;89(9):1069–101.

[57] Sevilla Ruben, Fernández-Méndez Sonia, Huerta Antonio. NURBS-enhanced finite element method (NEFEM). Arch Comput Methods Eng 2011;18(4):441–84.

[58] Legrain Grégory. A NURBS enhanced extended finite element approach for unfitted CAD analysis. Comput Mech 2013;52(4):913–29.

[59] Sun FL, Gong YP, Dong CY. A novel fast direct solver for 3D elastic inclusion problems with the isogeometric boundary element method. J Comput Appl Math 2020;377:112904.

[60] Yu Bo, Cao Geyong, Huo Wendong, Zhou Huanlin, Atroshchenko Elena. Isogeometric dual reciprocity boundary element method for solving transient heat conduction problems with heat sources. J Comput Appl Math 2021;385:113197.
[61] Wu YH, Dong CY, Yang HS. Isogeometric indirect boundary element method for solving the 3D acoustic problems. J Comput Appl Math 2020;363:273–99.
[62] Taus Matthias, Rodin Gregory J, Hughes Thomas JR, Scott Michael A. Isogeometric boundary element methods and patch tests for linear elastic problems: Formulation, numerical integration, and applications. Comput Methods Appl Mech Engrg 2019;357:112591.
[63] Beer Gernot, Mallardo Vincenzo, Ruocco Eugenio, Marussig Benjamin, Zechner Jürgen, Dünser Christian, Fries Thomas-Peter. Isogeometric boundary element analysis with elasto-plastic inclusions. part 2: 3-D problems. Comput Methods Appl Mech Engrg 2017;315:418–33.
[64] Sukumar N, Chopp DL, Moës N, Belytschko T. Modeling holes and inclusions by level sets in the extended finite-element method. Comput Methods Appl Mech Engrg 2001;190(46–47):6183–200.
[65] Du Chengbin, Ying Zongquan, Jiang Shouyan. Extended finite element method and its application in heterogeneous materials with inclusions. IOP Conf Ser Mater Sci Eng 2010;10:012083.
[66] Benowitz Brett A, Waisman Haim. A spline-based enrichment function for arbitrary inclusions in extended finite element method with applications to finite deformations. Internat J Numer Methods Engrg 2013;95(5):361–86.
[67] Song G, Yin HM. Stress concentration of one microvoid embedded in an adhesive layer under harmonic load. J Eng Mech 2018;144(3):04018002.
[68] Gao Xiaowei. 3D non-linear and multi-region boundary element stress analysis (Ph.D. thesis), University of Glasgow; 1999.
[69] Li Hong-Bao, Han Guo-Ming, Mang Herbert A. A new method for evaluating singular integrals in stress analysis of solids by the direct boundary element method. Internat J Numer Methods Engrg 1985;21(11):2071–98.